Lineage domains and cytoskeletal cables organize a cellular square grid in a crustacean

Beatrice L. Steinert[1,2,3], Leo Blondel[4,5], Chandrashekar Kuyyamudi[1,6], Evangelia Stamataki[7,8], Anastasios Pavlopoulos[7,8], Cassandra G. Extavour[1,4,6 *]

1 Department of Organismic and Evolutionary Biology, Harvard University
2 Department of the History of Science, Harvard University
2 Current address: Brown University
3 Department of Molecular and Cellular Biology, Harvard University
4 Current address: Learning Planet Institute, France
6 Howard Hughes Medical Institute
7 Institute of Molecular Biology and Biotechnology, Foundation for Research and Technology-Hellas, Heraklion, Greece
8 Janelia Research Campus, Howard Hughes Medical Institute, Ashburn, VA, USA

* Correspondence: extavour@oeb.harvard.edu

Abstract

To build tissues, and ultimately functional bodies, cells in early embryos must arrange into specific patterns. In most animals, epithelial tissues exhibit a predominantly hexagonal space-packing geometry. However, in many species of the largest group of crustaceans, the Malacostraca, the embryonic epithelium takes on the striking form of a grid made up of predominantly square cells, sequential rows of which establish the adult segmented body plan. After square cells emerge, their organization appears to be maintained by specific cell division patterns. However, the mechanisms that initially generate square cells from hexagonal precursors are unknown. Here we address this problem by combining long-term multiview lightsheet microscopy, immunohistochemistry, laser ablation, and pharmacological perturbation. We show that in the emerging model crustacean *Parhyale hawaiensis* this highly unusual grid geometry is first initiated from two perpendicular axes that are established sequentially according to different cellular mechanisms. The first axis arises dorso-ventrally at a tensile lineage compartment boundary, while the second emerges at the anterior-posterior axis along the ventral midline through lineage-independent cell intercalation driven by tensile actomyosin cables. We show that these midline cables are necessary for organizing square-cell packing as well as for proper expression of the segmentation gene *engrailed*. Our findings show that both cell lineage-specific behaviors, as well as lineage-independent supracellular structures, are required to establish square grid epithelial organization and a segmented body plan.

Keywords: amphipod, *Parhyale hawaiensis*, ectoderm, segmentation, epithelium, morphogenesis

43 # Introduction

44

45 The organization of cells and tissues during development is fundamental for multicellular
46 organisms. During embryogenesis, cells must be shaped at both the individual and collective tissue
47 levels to form functional structures at every stage of ontogeny. It has been appreciated since the
48 late nineteenth century that mechanical forces and geometric properties of cells and tissues play a
49 central role in morphogenesis, the generation of form during development[1]. Despite the
50 predominant focus on the role of genes in tissue patterning during the last half century[2–5], recent
51 decades have witnessed a resurgence of interest in the mechanics of development at the cell and
52 tissue scales of biological organization[6–8]. Harnessing techniques for live imaging and
53 computational image processing and annotation, recent work has begun to couple mechanical and
54 genetic contributions to tissue organization during embryogenesis[9]. However, these investigations
55 have been largely limited to a small number of model laboratory organisms, giving us a narrow
56 phylogenetic sampling.

57 The arthropods, which include insects and crustaceans, are and always have been the most
58 speciose group of animals on earth[10]. All arthropods have segmented body plans that are
59 established early in embryonic development[11]. Segmentation is evident in embryonic ectodermal
60 epithelia[12], tissues in which cells are tightly adhered to one another in a monolayer sheet and apical
61 cell faces form a confluent network of polygons[13]. Most epithelia that have been studied to date
62 are those in which constituent cells exhibit predominantly hexagonal packing with three-way
63 vertices, which is the geometry with minimal surface energy and maximal space-filling
64 efficiency[14–18]. During segmentation in the fruit fly *Drosophila melanogaster*[19,20] and the
65 milkweed bug *Oncopeltus fasciatus*[21], a small number of cells at segment boundaries briefly stray

66 from this geometry to give rise to an increased number of 4-way vertices, suggesting an altered
67 mechanical state. However, most epithelial cells retain their hexagonal shapes throughout
68 segmentation and early morphogenesis[22–24]. In *D. melanogaster*, maintaining boundaries between
69 embryonic segments requires tensile cables of actin and non-muscle myosin (myosin 2), which are
70 mechanically coupled across the tissue and prevent cell mixing across the boundary[19,24].

71 In contrast, in the early embryonic ectodermal epithelium of malacostracan crustaceans
72 (including shrimp, lobsters, isopods and amphipods) cells are packed into a grid of square cells[25,26]
73 arranged into highly ordered rows and columns[27,28]. Expression of the segment polarity gene
74 *engrailed* is initiated precisely every four rows of the square grid[29]. This emergence and
75 maintenance of square cells across the tissue is particularly striking given that higher surface
76 energy is predicted to be required for this space-packing geometry, and that 4-way vertices, which
77 are essential for square-packing, are unstable in vertex models of epithelia[30]. The amphipod
78 crustacean *Parhyale hawaiensis* is a powerful model for deepening our understanding of how local
79 lineage relationships and physical parameters of individual cells can result in correct tissue
80 morphogenesis and body patterning[31]. In contrast with *D. melanogaster*, in which early patterning
81 is set in motion within a syncytial embryo[32], the early *P. hawaiensis* embryo cleaves
82 holoblastically in a highly stereotyped manner that defines the cellular progenitors of all three
83 germ layers and the germ line as individual blastomeres of the 8-cell embryo[27]. From this stage
84 onwards, the three blastomeres that will give rise to the ectoderm–the descendants of which make
85 up the square-packing epithelium–can be tracked and their clones spatially mapped[27,33].

86 Here we uncover the cellular mechanisms underlying morphogenesis of this highly ordered
87 tissue in *P. hawaiensis*. Previous work in this amphipod suggests that after square cells appear,
88 their packing into a grid is maintained by cell divisions that occur in bilaterial, palindromic medial-

89 to-lateral mitotic waves during the phase when grid rows duplicate along the anterior-posterior
90 axis to establish clonally related parasegments[34]. However, the mechanisms that ensure that 4-way
91 vertices, square cells, and the tissue-wide arrangement of cells into rows and columns emerge in
92 the first place, remain unknown.

93 To address this problem, we used long-term, multiview lightsheet and confocal
94 microscopy, and imaged *P. hawaiensis* embryos from the 16-cell stage through to the first
95 emergence of square cells and the square grid (Fig. 1a). We used semi-automated cell tracking to
96 trace the ectodermal lineages and map their clonal domains onto the quantitative dynamics of cell
97 shape within the expanding epithelium. We show that square-packing geometry emerges along
98 two axes, corresponding with the anterior-posterior and dorsal-ventral body axes, through both
99 lineage-dependent and lineage-independent morphogenetic mechanisms within the tissue. We
100 further show that supracellular actomyosin cables form at these axes, and that the cables are under
101 locally-generated tension higher than that of the surrounding tissue. Finally, we provide evidence
102 that these cables function as a mechanical organizer of this tissue.

103

104 **Results**

105

106 *Ectodermal grid formation*

107 The first seven cleavages of the early *P. hawaiensis* embryo are holoblastic, and the progenitors
108 of all three germ layers and the germ line are established at the 8-cell stage[27,29,33,35]. Beginning at
109 approximately 20 hours post fertilization ("hpf" hereafter), cells that will contribute to the embryo
110 migrate towards the anterior pole and coalesce into an embryonic rudiment referred to as a "germ
111 disc," positioned atop yolk and surrounded by extraembryonic tissue (Fig. 1d). By 38 hpf, after

112 gastrulation (Fig. 1c-e, blue dotted line[33,36]), the ventral surface of this disc (Fig. 1f, h) consists of
113 a monolayer of ectodermal cells[15]. By 68 hpf, the cells in the germ disc have begun aligning into
114 rows and columns and transforming their apical faces into squares (Fig. 1i, j). This square grid sets
115 up the logic of segmentation of the adult body plan (Fig. 1g), with the conserved segment polarity
116 gene *engrailed* becoming expressed along its rows (Fig. 1i-k)[29,37].

117 To visualize this epithelial morphogenesis and its relationship to the ectodermal lineages
118 established at the 16-cell stage (Fig. 1b outside of blue dotted line, Supplementary Fig. 1a), we
119 generated volumetric, long-term timelapse images of *P. hawaiensis* embryos injected with nuclear
120 marker *H2B-mCherry* and plasma membrane marker *Lyn-EGFP* mRNA reporter constructs using
121 multiview lightsheet microscopy (Fig. 1a, Movies 1-2). We used a combination of manual and
122 semi-automated methods to annotate cell lineage, cell positions and mitotic activity throughout the
123 entire embryo in frames captured every ten minutes over more than 60 hours of development. We
124 captured the period starting from the eight cell stage at 9 hpf (Stage 4 as per Browne and
125 colleagues[29]) through to Stage 11[29] at approximately 70-74 hpf (Fig. 1a). By the end of the capture
126 period, the ectodermal grid of square cells that is the subject of this study is clearly established
127 (Fig. 1i, i'). We performed this annotation for three embryos, all of which hatched successfully
128 following imaging (Supplementary Table 1).

129 We wished to determine whether and how cell lineage, revealed by the tracking described
130 above, was related to the cell shape dynamics and rearrangements that establish the square grid
131 (Movie 3). However, in the later time-points of these datasets, when the germ disc has expanded
132 over the gradual curve of the embryo's surface, maximum intensity projections of the image
133 volume obscure apical cell morphologies and challenge accurate quantification of cell shape
134 dynamics. To solve this problem, we conformally mapped the 3D surface of the embryo onto a 2D

135 plane using the tissue cartography tool ImSAnE[34,38] (Fig. 1c'). To visualize the grid at even later
136 stages when the square-cell packing geometry has extended throughout the expanding ectoderm,
137 we dissected fixed embryos from the underlying yolk and physically flattened the ectoderm into
138 the 2D plane (Fig. 1h-k). The surface curvature of the unperturbed tissue at these stages is gradual
139 enough that, unlike in some large vertebrate embryos[39], flattening does not require incisions and
140 does not deform cell shapes. Using images of these flattened epithelia, we quantified the dynamics
141 of cell shape change in the ectoderm, as well as the relationship of these dynamics to the lineage
142 relationships of the constituent ectodermal cells, from the 16-cell stage through to the
143 establishment of the grid of square cells that serves as the template for the segmented body plan.
144
145 *Square-packing geometry initiates at a lineage compartment boundary*
146 Previous work has suggested that an ectodermal lineage compartment boundary runs perpendicular
147 to the anterior-posterior axis of the *P. hawaiensis* embryo[40]. Given the early stereotypic cleavage
148 patterns of this embryo, we asked whether lineage could contribute to the initiation of square-grid
149 morphogenesis. We tracked all six of the 16-cell ectodermal lineages (Era, Ela, Erp, Elp, Epr, Epl;
150 Supplementary Fig. 1a; nomenclature as per Gerberding and colleagues[27]) in the lightsheet
151 animations, enabling us to delineate the dynamic lineage territories within the developing germ
152 disc. We observed that a strict boundary emerged immediately after gastrulation between the
153 anterior (Eva, Ela, grey in Fig. 2a') and posterior (Erp, Elp, Epr, Epl, striped in Fig. 2a') lineages,
154 and that clones from each domain never crossed this boundary (Supplementary Fig. 1b, c). This
155 boundary, which we call the initiation line (IL, arrowheads in Fig. 2a), straightened into a line
156 perpendicular to the anterior-posterior axis by 68 hpf (Fig. 2b). The IL was made up of over 30%
157 4-way vertices from 38-56±2 hpf, and of over 40% 4-way vertices by 62±2 hpf (Fig. 2c). This

158 shows that the first emergence of large numbers of 4-way vertices, required for square cell
159 formation, is coincident with the formation of the IL, which is an ectodermal compartment
160 boundary.
161
162 *4-way cellular vertices first emerge in the local vicinity of the IL*
163 Given that 4-way vertices are essential for square cell-packing, and that such vertices first
164 appear in large numbers at the IL, we next characterized the emergence of square cells at the IL.
165 From 38-68 hpf, the cells near the IL exhibited extensive changes in shape and arrangement (Fig.
166 2a). The occurrence of cell rearrangement at the IL was evident by the dynamics of the four 16-
167 cell stage posterior ectodermal lineage domains (Erp, Elp, Epl, Epr; Supplemental Fig. 1a).
168 Whereas in the 26±2 hpf germ disc the Elp and Erp domains were on opposite sides (left and right)
169 of the germ disc, separated from each other primarily by descendants of the anterior Era and Ela
170 clones (Supplementary Fig. 1b, c, top row), they ultimately became separated by a single column
171 of posterior cells descended from one or both of Epl and Epr (Supplementary Fig. 1b, c, bottom
172 row). We also observed cell proliferation throughout the germ disc, including directly at the IL
173 and in the anterior and posterior compartments, throughout this time window (Supplementary Fig.
174 2, Supplementary Table 2).
175 To quantitatively describe the cell shape dynamics, including the transient changes in edge
176 numbers that result from a neighboring cell division and the instability of 4-way vertices[30], we
177 developed a cell shape descriptor metric, defined as the ratio of the area of a cell to the area of the
178 bounding circle of that cell. For this metric, values range from 0.5 to 1, where higher values are
179 closer to hexagons (Fig. 1l). We defined "square cells" as those with values in the range of 0.6-
180 0.66 (darkest color in Fig. 1l). We analyzed the changes in shape in cells along the IL (Fig. 2d, A1

181 and P1), and in cells one cell diameter away from the IL in both the anterior and posterior
182 compartments (Fig. 2d, A2 and P2). At 38 hpf, the rows immediately anterior (A1) and posterior
183 (P1) to the IL had more square cells (> 25%) than other measured regions (Fig. 2d). After 38 hpf,
184 P1 and the row one cell diameter anterior to the IL (A2) had the highest proportion of square cells
185 (20-25%) until 62 hpf, but by 68 hpf the proportion of square cells in A2 dropped to less than 20%
186 (Fig. 2d). The proportion of square cells immediately anterior to the IL (A1), and one cell diameter
187 away posterior to the IL (P2), was similar in both regions from 44 to 68 hpf (Fig. 2d). The
188 proportion of square cells in both regions increased by 68 hpf, comprising the highest proportion
189 of square cells of all measured regions. This gradual and local increase in square cells near the IL,
190 suggests that this lineage boundary initiates and maintains the transition to square-packing
191 geometry along the dorsal-ventral axis.
192
193 *A simulation of cell sorting can explain the emergence of the IL as a straight boundary*
194 Given that the IL is a lineage compartment boundary, we asked whether and how lineage might
195 contribute to the emergence of this first grid axis, which becomes increasingly straight from 26-
196 68 hpf (Fig. 2a, Supplementary Fig. 1b, c). To test the hypothesis that minimization of interfacial
197 free energy at the boundary between cells of distinct ectodermal lineages might be responsible for
198 boundary formation, we used CompuCell3D[41–43] to simulate cell sorting within the *P. hawaiensis*
199 ectoderm. To obtain biologically realistic parameters for this simulation, we first segmented
200 lightsheet images at 26 hpf, the first time point after the completion of gastrulation, when the
201 surface epithelium is made up entirely of ectoderm cells (Figs. 2a, 3d, Supplementary Fig. 1b). We
202 then quantified the number of cell divisions within each of the six 16-cell stage ectodermal lineages
203 (Fig. 3a) up to 20 hours after this time point (46 hpf). The membrane segmentation and lineage

204 proliferation rates, as well as increased contact energy between the anterior and posterior lineages
205 (Fig. 3b'), were the initial conditions for the simulation. When run, the model consistently (n = 10
206 runs) produced a straight anterior-posterior compartment boundary as well as a clonal domain
207 mapping like those observed in the actual tissue (Fig. 3e; compare with Supplementary Fig. 1b, c,
208 bottom row). As observed in living embryos (Supplementary Fig. 1b, c), descendants of anterior
209 (Era, Ela) and posterior (Erp, Elp, Epr and Epl) ectodermal founder cells in our model became
210 increasingly mixed with each other anterior and posterior to the IL respectively (Fig. 3c, groups I
211 and II). In contrast, cells on either side of the IL became increasingly segregated over the analyzed
212 time course (Fig. 3c, group III). The results of the model are consistent with the hypothesis that
213 the IL represents a stable compartment boundary arising from the principle of energy minimization
214 between clones of anterior and posterior cells.
215
216 *A midline of square cells forms the secondary axis of the grid through intercalation*
217 Previous clonal analyses across multiple species of malacostracan crustaceans have shown that a
218 morphologically distinct column of cells forms along the ventral midline of the embryo[26,27,44–48].
219 The cells of the midline were previously reported to be entirely comprised of Ep descendants
220 (Supplementary Fig. 1a) in *P. hawaiensis*[27], but are described as a polyclone descended from
221 multiple 8-cell stage ectodermal precursors in the related amphipods *Orchestia cavimana*[46,49] and
222 *Gammarus pulex*[45]. We asked whether the *P. hawaiensis* midline played a role in square-cell
223 packing along the anterior-posterior axis of the ectodermal grid, and whether its formation was
224 lineage-dependent. We observed that *P. hawaiensis* midline formation began at 50-60 hpf through
225 sequential mediolateral intercalation[50] of a founder cell population (Fig. 4a-b) in a region we call
226 the intercalation zone (IZ, Movie 4, Fig. 4a'-a''', Supplementary Fig. 3c, d). This region

227 subsequently split into anterior and posterior intercalation zones (Fig. 4a''-a'''), defined as regions
228 of intercalation anterior (IZA) and posterior (IZP) to the IL respectively, as cells aligned at the
229 midline. The IZ founder cell population was identified in the lightsheet datasets by tracking the
230 lineages of aligned cells at 68-70 hpf backwards to the point when only one midline cell was
231 aligned. For the next 10 to 12 hours, the midline elongated (Fig. 4b', c', Supplementary Fig. 3e, f)
232 by a combination of mitotic divisions within the founder population (Fig. 4b', 9-cell midline) and
233 cell intercalation. Midline intercalation started at the IL (arrowheads in Fig. 4a'-a''',
234 Supplementary Fig. 3c-f) and progressed both anteriorly and posteriorly, with the accumulation of
235 midline cells in the anterior zone lagging behind that in the posterior (Fig. 4c). Cells were added
236 to the midline sequentially (Fig. 4c', Movie 4) and each new cell added took its final shape as a
237 square only once it was entirely within the midline (Fig. 4b'). Once aligned, midline cells remained
238 square and were the first square cells formed along the anterior-posterior axis of the grid (Fig. 4a'-
239 a''', Supplementary Fig. 3e, f). To the left and right of this axis, the remaining ectodermal cells
240 first aligned and subsequently transitioned to square-packing in a medio-lateral wave initiated from
241 the midline (Fig. 4a"-a'''). After the 10-12 hour period of midline elongation by intercalation and
242 founder cell division, by 60-72 hpf the midline contained a mean of 8.75 cells in total (Fig. 3c).
243 Subsequently, divisions of parasegment precursor rows[29] in the posterior compartment introduced
244 another mechanism of further midline elongation (starred cells in Fig. 4a"-a''').

245 In contrast with the initiation line, the midline grid axis did not strictly correspond to clonal
246 boundaries between 16-cell ectodermal lineage domains (Supplementary Fig. 3). The emergence
247 of the midline, with the same cell behaviors extending it in both directions along the anterior-
248 posterior axis, spanned the anterior and posterior lineage domains (Fig. 4b, Supplementary Fig.
249 3c, d). However, we observed that the posterior midline was not exclusively made up of Ep

250 descendants (Supplementary Fig. 3c). This is in disagreement with the original lineage tracing
251 report for *P. hawaiensis*[27], but is consistent with the report that embryos lacking an Ep blastomere
252 still form a midline[40]. In the anterior portion of the midline, clones from both anterior ectodermal
253 lineages (Era and Ela) contributed to the midline founder population with no apparent relationship
254 between lineage domains and the anterior IZ (Supplementary Fig. 3a, b). Taken together, these
255 results suggest that the midline initiates the emergence of complete square cells and square-cell
256 packing along the anterior-posterior axis through a highly coordinated morphogenetic process
257 based on cell recruitment rather than inherited fates, as it is not dependent on the 16-cell stage
258 ectoderm lineages (Supplementary Fig. 3).
259
260 *The initiation line and midline column form tensile cytoskeletal cables*
261 Given the emergence of square-cell packing geometry first at the IL (around 30 hpf) and
262 subsequently at the midline (around 50 hpf), we hypothesized that these boundaries introduce
263 tension into the tissue to initiate the transition to square-packing. To test this hypothesis, in *P.*
264 *hawaiensis* embryos stained with phalloidin (Fig. 5a) and injected with a myosin 2 mRNA reporter
265 construct (based on the *P. hawaiensis* ortholog of the *D. melanogaster* gene encoding the
266 regulatory light chain of the non-muscle type 2 myosin, known as *spaghetti-squash* [51] (*Ph-sqh*),
267 Supplementary Fig. 4), we measured the relative amounts of filamentous actin (F-actin) and
268 myosin 2 at the IL when it appeared in earlier stages (38-56 hpf, Fig. 5a-a'), and on either side of
269 the midline when it formed at later stages (around 68-74 hpf, Fig. 5b, b').
270 In 38-56 hpf embryos, we found significantly higher levels of F-actin (Fig. 5a, a') and
271 myosin 2 (Supplementary Fig. 4a, a') at the IL relative to the equivalent region of interest (ROI)
272 one cell anterior (IL/A1) or posterior (IL/P1), compared with one to two cells posterior (P1/P2).

273 Similarly, we also found significantly higher levels of F-actin on the left (ML) and right (MR)
274 sides of the midline in embryos with 6-15 cells in the midline (68-74 hpf) (Fig. 5b, b') compared
275 with the equivalent ROIs one and two cells to the left (ML1, ML2) and right (MR1, MR2). In
276 contrast, levels of myosin 2 on either side of the midline were not significantly higher than the
277 ROIs to the left and right of the midline (Supplementary Fig. 4b'b"). We hypothesize that these
278 accumulations of cytoskeletal proteins constitute supracellular cables running along the two axes
279 of the ectodermal grid (Supplementary Fig. 5).

280 In *D. melanogaster*, actomyosin cables segment embryonic and larval tissues by
281 introducing local tension into the tissue[19,52,53]. We hypothesized that the supracellular cables we
282 detected in the *P. hawaiensis* germ band were similarly under tension, allowing them to regulate
283 the formation of the first square cells in the grid. To test this hypothesis, we cut the cables with a
284 pulsed laser tuned to 927 μm and measured subsequent tissue recoil around the incision site (Fig.
285 5c, dashed line and arrows). In 38-44 hpf embryos that had formed the IL, recoil speeds were
286 significantly (1.5 to 2.5-fold) higher at the IL compared with control cuts made four to seven cells
287 anterior to the IL (Fig. 4c'). Interestingly, this increase is comparable to the mean of 2.37-fold
288 higher tension reported at the *D. melanogaster* wing disc anterior-posterior compartment boundary
289 compared with that at cell edges within the anterior or posterior tissue compartments[52]. In embryos
290 live-imaged following the IL cut, we observed that the 4-way vertices surrounding the incision site
291 remained intact (black arrowheads in Fig. 5c), suggesting that maintaining a square shape at the
292 IL is not dependent on tension in neighboring cells.

293 In later stage embryos in which 3-6 cells had aligned into the midline (58-69 hpf), recoil at
294 midline cables in the posterior IZ was significantly (2 to 3-fold) higher than at other non-IZ regions
295 one to four cell diameters anterior or lateral to the midline (Fig. 4c"). In contrast, recoil speeds at

296 the cables in the anterior region of the midline where intercalation had finished and cells were
297 square in shape (P1 in Fig. 5b, c") were not significantly different than those at the lateral and
298 anterior control regions (Fig. 5c"). To determine whether tension was mechanically coupled across
299 cells contributing to the cable, we measured the recoil of a second cut in the midline after making
300 a first cut two to three cells away in the cable (Fig. 4c'), and found that P1 and IZ second cut
301 recoils were not significantly different from those at first cuts (Fig. 5c"). We note that a similar
302 phenomenon of local, potentially cell-autonomous contribution to tension across a supracellular
303 actomyosin cable spanning many cell diameters, has also been reported in the morphogenesis of
304 an extra-embryonic membrane in the beetle *Tribolium castaneum*[54]. Taken together, these results
305 suggest that there are supracellular cables under tension at the IL and at the midline, and that
306 tension within midline cables is heterogeneous and locally generated.

307 Tension in actomyosin cytoskeletal cables results from the phosphorylation of the
308 regulatory light chain of myosin 2, which slides the attached actin filaments past one another[55].
309 The results of our laser ablation experiments suggested that while both the IL and the midline
310 cables possessed supracellular actomyosin cables that were under tension, tension at IL was not
311 essential for the formation of 4-way vertices. This led us to hypothesize that abrogation of myosin
312 2 phosphorylation would not hinder square cell-packing geometry formation at the IL at earlier
313 stages, but might disrupt square cell formation at the midline at later stages.

314 To test this prediction, we first assessed the effect of sustained elimination of myosin 2
315 phosphorylation during the later stages. We focused on the period when intercalation is the only
316 mechanism of midline formation (50-68 hpf, Fig. 4b, b'), and chose morphologically stage-
317 matched embryos in which just one cell had aligned into the midline (50-56 hpf, Fig. 4b) for
318 incubation in 50μM of the Rho-kinase inhibitor Rockout for 12 hours (Fig. 5d, d'). This

319 concentration of Rockout did not impact normal cell proliferation (Supplementary Fig. 6a, b),
320 thereby allowing the thresholds of contractility needed for cytokinesis[19,53]. Rockout-treated
321 embryos at this stage had significantly fewer cells aligned into the midline than controls (mean 1.4
322 vs 6.4, Fig. 5f) but maintained the same total number of cells in the posterior compartment (Fig.
323 5f'). Notably, a relatively straight boundary at the IL was maintained in the midline Rockout-
324 treated embryos (Fig. 5d', arrowheads). In contrast, earlier stage embryos (38 hpf) treated for 12
325 hours in 50µM Rockout had, by 50 hpf, percentages of 4-way vertices that were not significantly
326 different from controls (Fig. 5e). Taken together, these results suggest that while 4-way vertices
327 first appear at the IL (Fig. 2), their maintenance is not dependent on the phosphorylation of myosin
328 2 (Fig. 5e). In contrast, however, subsequent establishment of the first square cells is dependent
329 on the contractility of myosin 2 within midline cables (Fig. 5g).
330
331 *The midline cables organize square-cell packing and the emergence of a stripe of Engrailed-*
332 *positive cells*
333 Given the presence of differential tension within the germ disc (Fig. 5c, c"), and the midline as the
334 initiation site of the transition to square-packing along the axis of grid elongation (Fig, 4,
335 Supplementary Fig. 3), we hypothesized that localized mechanical perturbation of the midline
336 would disrupt the organization of square-cell packing across the tissue, and that perturbing square-
337 cell packing would in turn have consequences for the correct establishment of segments. To test
338 this, we performed two classes of physical ablations, either directly at the midline (Mid), or three
339 cell diameters lateral to the midline (Lat) in embryos in which 3-6 midline cells had aligned (58-
340 69 hpf, A: pink rectangles in Fig. 6b, c). The contralateral side of the same embryo, which was not
341 ablated (NA: pink rectangles in Fig. 6b, c), served as an internal control. In the resulting four

342 experimental groups (Mid-A, Mid-NA, Lat-A, Lat-NA), we analyzed posterior compartment cell
343 shapes (Fig. 6d, d'), number of cells in the midline (Supplementary Fig. 7), and expression of the
344 segment marker Engrailed[37] (En, Fig. 6e, Supplementary Table 3) 9-12 hours after ablation. In the
345 100 closest cells to P1 posterior to the IL, we used Kernel density estimation[56,57] to estimate the
346 cell shape probability densities for all groups, including wild type embryos morphologically stage-
347 matched to Lat embryos based on the number of cells in the midline. We plotted the deviation of
348 the four experimental groups from the wild type distribution over the range of cell shape values
349 observed (Fig. 6d').

350 We found that at 38 hpf, ablations of the IL and control ablations three cell diameters
351 anterior to the IL did not prevent the formation of square cells nor the establishment of the
352 ectodermal square grid (Supplementary Fig. 8). Additionally, 38 hpf embryos in which we made
353 a single cut in the IL cable maintained a straight line at the IL region of the tissue and began
354 midline formation 12 hours later (Supplementary Fig. 8). This is consistent with the observation
355 that 4-way vertices still form correctly after inhibition of myosin 2 phosphorylation at IL
356 establishment stages (Fig. 5e).

357 In contrast, in embryos in which 3-6 midline cells had aligned (58-69 hpf), ablations lateral
358 to the midline significantly perturbed the cell shape distribution on the ablated side of the embryo
359 (Lat-A, Fig. 6d) compared with the unablated side (Lat-NA), overall driving them towards a
360 rounder, rather than square, shape (Fig. 6b', d'). Relative to wild type, Lat-NA exhibited the
361 smallest increase in anisotropic cells (defined as those with a cell shape metric value of $\leqslant 0.5$;
362 circle (i) in Fig. 6d') and the smallest decrease in square cells (circle (ii) in Fig. 6d') of all four
363 groups.

364 Unlike the localized impact of lateral ablations, midline ablations significantly disrupted
365 cell shape distributions both on the ablated side (Mid-A) and on the contralateral control side (Mid-
366 NA) (Fig. 6c',d'). On both sides of midline ablated embryos, more cells took on more irregular
367 shapes, characterized by lower values of the cell shape metric (Fig. 6d). In particular, the
368 proportion of square cells was lower than wild type in both the experimental and the control
369 (contralateral) group of midline ablations (circle (ii) in Fig. 6d'). Midline ablation destroyed the
370 organization of the square-packed grid throughout the posterior germ rudiment (Fig. 6c'). In sum,
371 the effect of the lateral ablation was minimal and localized to the region immediately around the
372 ablation, while perturbing just one of the midline cables had a tissue-wide impact on cell shapes,
373 disrupting square cell formation and abolishing the square ectodermal grid.

374 Midline, but not lateral, ablations also disrupted midline elongation. Laterally-ablated
375 embryos developed midlines with total numbers of cells comparable to wild type (12-19 cells,
376 Supplementary Fig. 7) while midlines in midline-ablated embryos were shorter (5-10 cells,
377 Supplementary Fig. 7). This suggests that midline cable ablations, but not ablations lateral to the
378 midline, disrupted posterior intercalation at the midline. These data are consistent with the
379 hypothesis that the alignment of cells into the midline, driven by the contractility of the midline
380 cables, organizes cell shape across the tissue.

381 Finally, we asked whether establishment or maintenance of the square cell grid was
382 important for correct (para)segment patterning. At stage 11-12 of embryogenesis (66-68 hpf[29]),
383 when midline elongation by intercalation has completed (Fig. 4a"), the protein product of the
384 segment polarity gene *engrailed* (En) becomes detectable in two cells anterior to the IL, initially
385 in a few cells within the same row at or near the midline[29]. The En expression domain subsequently
386 expands in an increasing, left-right symmetrical number of lateral cells within the row[29]. This

387 expression marks the prospective mandibular segment (Mn, arrowhead in Fig. 1i, j)[29,44].
388 Subsequent rows of En-expressing ectodermal cells, delineating the remaining segments of the
389 body plan, arise correlated with the same stereotyped cell divisions of the cells in the grid that
390 contribute to midline elongation (Fig. 1j, k) [29,44].

391 Given that En expression in the prospective mandibular segment is detected right after the
392 midline intercalation phase that appears to create the first square cells in the grid, we asked whether
393 this expression was dependent on the tensile midline cables in the same way as square cells and
394 square-packing order. Across the WT and ablated samples, we found that the total number of
395 Engrailed-positive nuclei in the prospective mandibular segment was positively correlated with
396 the number of aligned midline cells (Supplementary Fig. 7b, Supplementary Table 3). In other
397 words, as the midline became longer, more lateral cells within Mn expressed En. Strikingly,
398 however, midline ablation reduced the number of En-positive Mn nuclei, even on the contralateral
399 control side of the embryo (Figure 6e, Supplementary Table 3). In contrast, lateral ablations had
400 little impact on the number of Engrailed-positive Mn nuclei on either the experimental or the
401 control side of the embryo (Figure 6e, Supplementary Table 3). Midline but not lateral ablations
402 also decreased the regularity with which Mn cells expressed En (Figure 6e, Supplementary Table
403 3). Given these results, we hypothesize that the first establishment of En expression across a
404 complete segment, as seen in Mn, requires midline-cable driven tissue organization.
405

406 **Discussion**

407

408 *The role of cell lineage in initiating square cell formation*

409 We found that descendants of the 16-cell stage ectodermal founder blastomeres segregate into
410 anterior and posterior compartments, and that the resulting compartment boundary (IL) forms the
411 first axis of the square cell grid. This suggests the possibility that cell lineage at least partly
412 underlies square cell morphogenesis. The results of our simulation suggest that cell sorting
413 between the cells of the anterior and posterior compartments, a phenomenon observed in multiple
414 contexts in animal development including amphibian embryos[58] and *Drosophila* imaginal discs[59],
415 regulates the formation of a straight compartment boundary. The mechanism that regulates this
416 cell sorting could in principle be one or more of differential cortical stiffness[60–62], differential
417 adhesion[61–67], or a mechanical barrier imposed by the supracellular actomyosin cable that forms at
418 the IL. Relevant to the latter hypothesis, we note that although the cable at the IL is under tension,
419 coupled tension and the phosphorylation of myosin 2 are not required to maintain 4-way vertices
420 at this boundary. This suggests that local tension at this IL cable is not necessary to maintain the
421 compartment boundary. Alternatively, it is possible that the interaction between the anterior and
422 posterior lineages can restore the tensile cable upon ablation.

423 The results of previous experiments demonstrating that the *P. hawaiensis* early embryonic
424 ectoderm has regulative capacity are interpretable as consistent with the cell sorting hypothesis[40].
425 In these experiments, individual 8-cell stage ectodermal blastomeres were photoablated and the
426 remaining two blastomeres were injected with a lineage tracer. The results showed that El and Er
427 can replace each other's anterior descendants, while Ep can replace their posterior descendants[40].
428 We hypothesize that compensation within the ectoderm, and ultimately grid formation, is possible
429 only when progenitors of both anterior and posterior lineages remain, and that cells from both
430 compartments are necessary to initiate square cell-packing geometry at the IL. Under this
431 hypothesis, both anterior and posterior cell types would be needed to form the boundary because

432 each lineage would contribute a distinct molecular state (e.g. cortical stiffness and/or adhesive
433 properties), the combination of which would then lead to emergent cell sorting.

434 In embryos of diverse animal species–including *D. melanogaster*[68–70], the flour beetle
435 *Tribolium casteneum*[54], the cnidarian *Hydra vulgaris*[71], the zebrafish *Danio rerio*[72], and the quail
436 *Coturnix japonica*[73]–mechanically integrated actomyosin cables spanning multiple cells play
437 crucial roles in epithelial morphogenesis. We hypothesize that differential genetically-determined
438 fate between the anterior and posterior lineages also underlies the assembly, and potentially the
439 shape organizing function, of the cytoskeletal cable we observed at the anterior-posterior boundary
440 (IL) from 38 hpf onwards, similar to anterior-posterior boundary formation in the *D. melanogaster*
441 wing disc[52]. In the early *Caenorhabditis elegans* embryo, both endodermal cell fate and the
442 phosphorylation of myosin 2, which are necessary for gastrulation in endodermal cells, are
443 dependent on the Wnt-Frizzled signaling pathway, suggesting a direct connection between cell
444 fate and morphogenesis[74]. A similar relationship could exist within the *P. hawaiensis* ectoderm,
445 the molecular determinants of which have yet to be identified.

446 Further ablation experiments in 16-cell stage embryos that eliminate all anterior or
447 posterior lineages, or elucidation of the transcriptomic, proteomic and mechanical states of the
448 anterior and posterior compartment clones, would be useful to elucidate the mechanism of cell
449 sorting at the IL. A hypothesis of one or both of differential adhesion or differential cortical
450 stiffness would predict that anterior and posterior cells have different levels of cell-cell adhesion
451 molecules and/or different cortical cytoskeletal behaviors. The fact that the IL marks a clonal
452 boundary could in principle provide a heritable mechanism of achieving differential molecular
453 states between clones. For example, anterior cells might inherit a level of adhesion molecules or a

454 cortical cytoskeletal conformation distinct from that of their posterior neighbors by virtue of
455 differential inheritance of cytoplasmic factors, or through inheritance of a gene regulatory state.
456
457 *Lineage dependent and lineage-independent mechanical cues establish square cell packing*
458 Once the IL has straightened into an actomyosin rich boundary axis, we found that a
459 midline cell founder population begins to intercalate perpendicular to the IL such that square cells
460 are added sequentially to the midline between two actomyosin cables. This grid axis does not
461 correlate with 16-cell lineage domain boundaries, such that the midline founder population is a
462 polyclone containing descendants of multiple ectodermal founders (Supplementary Fig. 1, 2).
463 These findings suggest that, unlike the IL, the formation of the midline and its cables is not
464 regulated by inherited differences among these lineages. We hypothesize that the midline grid axis
465 is instead initiated by mechanical stimuli, similar to how the formation of the primitive streak in
466 early avian embryos, which involves anterior-posterior oriented actomyosin cables[75], is driven by
467 tissue flows that regulate the expression of fate-determining genes.[9] Under this hypothesis, the
468 midline founder population would become defined–and, in turn, potentially genetically
469 differentiated–as a result of tissue-wide forces. Future work could examine whether fate-
470 determining genes of this population include components of the planar cell polarity signaling
471 pathway, which is involved in medio-lateral intercalation of cells in multiple developmental
472 contexts.[76–80]
473 We have provided evidence that the mechanical integrity of these midline cables is
474 necessary for the formation of isometric cells, the alignment of cells into rows, the maintenance
475 and packing of square cells across the ectodermal grid, and the establishment of segmentally
476 iterated En expression. We hypothesize that these cables drive tissue-wide mechanics, just as tissue

477 flows pattern the retina[81] and embryonic germ band extension[82] in *D. melanogaster*, or how
478 supracellular actin cables organize whole body regeneration in *H. vulgaris*[71]. In this framework,
479 the tension introduced by the midline cables at the intercalation zones could be the initial condition
480 necessary to trigger and perhaps subsequently balance the transition to square-packing. The
481 variance in recoil times in response to ablation at the IL and midline intercalation zones (Fig. 5c',
482 c"), suggests that tension at these regions could be dynamically modulated in response to global
483 tissue forces.
484
485 *The relationship between square-cell packing, gene expression, and segmental patterning*
486 In ascidian and mouse embryos, cell geometry is crucial for the expression of fate-determining
487 genes[83,84]. Our study suggests that in *P. hawaiensis*, square grid morphogenesis and subsequent
488 segment formation emerge from axes that are established according to differing degrees of
489 instruction from tissue mechanics and genes. We also provide evidence that expression of the
490 segment polarity gene *en* in the *P. hawaiensis* ectoderm is sensitive to mechanical perturbation
491 and dependent on the formation of the midline. Reminiscent of this finding, in *D. melanogaster*
492 embryos injected with paramagnetic-beads and subjected to ectopic tissue-wide forces with
493 magnetic tweezers, expression of En at parasegment boundaries was differentially altered
494 according to the location and magnitude of the force[85]. The authors of that study observed a change
495 in nuclear shape and redistribution of myosin 2 in tissue regions experiencing the applied force,
496 suggesting that expression of *en* is downstream of these mechanical and geometric parameters[85].
497 This raises the possibility that mechanical regulation of *en* expression could be a conserved feature
498 in multiple pancrustacean species.

499 In early *D. melanogaster* embryos, membrane fluidization by an ether treatment applied to
500 whole embryos results in larvae with a dramatic range of segmentation defects, from complete loss
501 of segments to the elimination of only a single segment, which resembles segmentation gene loss
502 of function phenotypes[86]. Our *P. hawaiensis* midline ablation experiments, in which cuts were
503 made in the exact same cell positions across samples, similarly resulted in a range of changes in
504 cell shape, midline cell number, and *en* expression, suggesting that segmentation in *P. hawaiensis*
505 could arise from a balance of tuned forces within the ectodermal epithelium. In this mechanical
506 framework, the ultimate effect of midline cable disruption could depend on the mechanical state
507 elsewhere in the tissue. Further experiments determining the longer-term effect of early midline
508 disruption, and the alteration of square-cell packing, on the formation of more posterior segments
509 will be necessary to establish the extent of the midline cables' organizing capabilities.

510 Beyond amphipods, previous comparative studies of embryogenesis in other malacostracan
511 orders (including Cumacea, Tanaidacea, Isopoda, and Mysidacea) have found that they generate
512 some of the cell material for their ectodermal grids through consecutive divisions of ectodermal
513 stem cells (ectoteloblasts) that provisionally align their clonal progeny into rows in the posterior
514 portion of the grid[87]. However, ectodermal grids in these species also contain cells derived from
515 non-ectoteloblast lineages, suggesting that some other mechanism of tissue organization must be
516 present[28]. Amphipod grids like that of *P. hawaiensis* completely lack ectoteloblasts and thus must
517 be organized by what Wolfgang Dohle and Gerhard Scholtz called a "row-forming factor," which
518 they hypothesized to be a "matrix forcing the cells into a grid-like pattern"[87]. Our results suggest
519 that this "matrix" emerges first from tensile cell-sorting at the IL and subsequently from
520 cytoskeletal cables at the midline. *O. cavimana*, another amphipod, exhibits stereotypic early
521 cleavage patterns similar to that of *P. hawaiensis*, suggesting that fate determination within the 8-

522 16 cell embryo could also play a role in grid morphogenesis of this species[46]. Further lineage
523 studies across the Amphipoda, the early embryos of which all undergo holoblastic cleavage[88], are
524 needed to understand the full extent of this mechanism within this group.

525 The amphipod anterior-posterior compartment boundary corresponds to a boundary
526 classically called the naupliar-post-naupliar boundary. Under this concept, the naupliar region of
527 the germ band, is the anterior region that will give rise to the head and mandibular segments,
528 formed through a combination of relatively uncoordinated mitoses, cell intercalation, and cell
529 rearrangements, and the post-naupliar region. In contrast, the post-naupliar germ band is formed
530 through the activity of either ectoteloblasts or segment precursor row duplications[44,45,89], and gives
531 rise to the trunk segments and telson. Interestingly, our work shows that the IL, positioned one cell
532 diameter posterior to the first complete segmental stripe of En expression in the prospective
533 mandibular segment, corresponds to the classically defined naupliar-post-naupliar boundary.

534 The anterior-posterior compartment boundary is established by the descendants of
535 ectodermal lineage precursors defined by stereotypical holoblastic cleavages[27,33] and likely also
536 by asymmetric inheritance of lineage potential to early blastomeres that begins at first
537 cleavage[35,90,91]. However, holoblastic cleavage is a derived state for the Malacostraca, in which
538 many extant species undergo syncytial cleavage[46], and the ancestral cleavage state is thought to be
539 meroblastic (in which cleavage furrows form but cytokinesis is not completed, effectively resulting
540 in a syncytium but with some partial yolk partitioning by the formation of incomplete furrows)[92,93].
541 We speculate that the evolution of holoblastic cleavage in amphipods facilitated the emergence of
542 lineage-based IL formation and the anterior-posterior compartment boundary as a mechanism for
543 establishing the ectodermal grid and generating the post-naupliar germ band. Under this
544 hypothesis, the evolution of an anterior-posterior boundary among the ectoderm clones eliminated

545 the need for patterning introduced by a row of proliferating ectoteloblasts within the germ disc.
546 With regards to grid organization along the anterior-posterior axis, we hypothesize that midline
547 formation via intercalation, and the importance of the mechanical organizing properties of the
548 midline for establishing correct segmental patterning, are likely to be conserved across the
549 Malacostraca. Further comparative studies should determine whether midline cables are present in
550 other species.
551
552 **Methods**
553
554 *Animal culture and transgenesis*
555 *P. hawaiensis* were cultured at 26 ºC in 16-quart plastic tanks containing 1.022 specific gravity
556 Instant Ocean artificial sea water (hereafter ASW) made with distilled water and fed a diet of
557 TetraPro PlecoWafers and fresh carrots. For live imaging of nuclei (Fig. 4c) we used a previously
558 reported[94] transgenic *P. hawaiensis* line in which the *D. melanogaster* histone H2B fused with a
559 monomeric Red Fluorescent Protein is under control of a *P. hawaiensis* heat-shock promoter
560 (hereafter *H2B-mRFPruby*).
561
562 *Embryo collection and microinjection*
563 Embryos for all experiments were collected and microinjected according to established
564 protocols[95]. Embryos were collected into and cultured in ASW filtered with a 0.22µm filter
565 (hereafter FASW). For precise staging and stage-matching among broods, only 1-cell through 8-
566 cell stage embryos were collected. All microinjected embryos were injected at the late 1-cell stage
567 once the chorion had hardened. Microinjected embryo cultures were supplemented with 1:100

568 Penicillin-Streptomycin (10,000 U/mL penicillin, 10,000 µg/ml streptomycin; Gibco 15140-122)
569 and 1:200 Amphotericin-B (250 µg/ml, Gibco 15290-026). The culture medium was changed out
570 every 1-2 days. For live imaging of the actomyosin cytoskeleton, embryos were injected with
571 180pl of 2 µg/µl of mRNA reporter constructs encoding either the actin-binding peptide LifeAct[96]
572 fused to the monomeric mNeonGreen fluorescent protein[97] (hereafter *LifeAct-mNeonGreen* or *LA-*
573 *mNG*) or the *P. hawaiensis* myosin II regulatory light chain gene (*Ph-sqh*) fused to mNeonGreen
574 (hereafter *Ph-sqh-mNG*). In vitro transcribed capped mRNAs encoding these reporters were
575 synthesized with the mMessage mMachine T7 kit (Invitrogen AM1344) from plasmid templates
576 pBlueSK-LifeAct-mNG and pBlueSK-Phsqh-mNG linearized with the restriction enzyme NotI, as
577 previously described (Kontarakis 2014). Plasmid templates pBlueSK-LifeAct-mNG and
578 pBlueSK-Phsqh-mNG were generated by PCR amplification of the *LA-mNG* and the Ph-sqh-mNG
579 open reading frames (with primer combinations pBlue_LA_GBS_F 5'-
580 agaactctgggggatctgatAatgGGCGTGGCCGATC-3' / pBlue_mNG_GBS_R 5'-
581 cggttcagaacttataacaTTACTTGTACAGCTCGTCCATG-3' or pBlue_Phsqh_GBS_F 5'-
582 agaactctgggggatctgatAATGTCGTCCCGCAAAGC-3' / pBlue_mNG_GBS_R) from vectors
583 pSL-PhHS-LA-mNG and pSL-PhHS-Phsqh-mNG, respectively (Kalogeridi and Pavlopoulous,
584 personal communication). PCR amplicons were cloned with Gibson assembly into ClaI-digested
585 pBlueSKMimRNA[98], replacing the Minos transposase ORF with the LA-mNG or the Ph-sqh-
586 mNG ORFs, respectively. For long-term lightsheet imaging of cell membranes and nuclei,
587 embryos were co-injected with in vitro transcribed capped mRNAs synthesized with the
588 mMessage mMachine SP6 kit (Invitrogen AM1340) either from plasmid template pEXPTol2-
589 H2A-mCherry (encoding the nuclear fluorescent reporter H2A-mCherry) linearized with the

590 restriction enzyme BglII[99] or from plasmid template PCS2 + Lyn-EGFP (encoding the membrane
591 fluorescent reporter Lyn-EGFP) linearized with the restriction enzyme NotI[100] .
592
593 *Immunohistochemistry and drug treatments*
594 Embryos were dissected away from their outer membrane according to established protocols[101]
595 and fixed for one hour at room temperature in 4% paraformaldehyde made up in FASW. Fixed
596 tissue was immediately transferred into a blocking solution (1x phosphate buffered saline (1x PBS)
597 + 5% normal goat serum + 0.1% Triton X-100) or stored at 4 ºC in 1x PBS + 0.1% Triton X-100
598 for up to three days prior to staining. Embryos were stained with 1:100 AlexaFluor 488 Phalloidin
599 (Invitrogen A12379) or Rhodamine Phalloidin (Invitrogen R415) for F-actin, 1:1000 rabbit anti-
600 Myosin 2 656[102], 1:80 mouse anti-Engrailed Mab 4D9[37], 1:500 mouse anti-phospho-histone H3
601 (Cell Signaling 9706S), or 1:50 rabbit anti-cleaved caspase-3 conjugated to AlexaFluor 555 (Cell
602 Signaling 9604S) overnight at 4ºC. We followed these incubations with a solution containing
603 1:10,000 Hoechst 33342 (Sigma B2261, 10 µg/µl stock solution) as well as secondary antibodies
604 1:500 AlexaFluor 647-conjugated Goat Anti-Mouse (Invitrogen A31625) or 1:500 AlexaFluor
605 555-conjugated Goat Anti-Mouse (Invitrogen A31621) in blocking solution for two hours at room
606 temperature. Prior to fixation, drug-treated embryos were cultured for 12 hours at 26ºC in a
607 solution of Rockout (Rho Kinase Inhibitor III, Sigma 55555-3) dissolved in anhydrous DMSO and
608 added to a 30mm petri dish containing 6ml of 50% FASW, as previously described[36]. We found
609 that a 50µM concentration of Rockout did not disrupt normal cell proliferation and that 100% of
610 38 hpf-treated embryos survived up to two days in a continuous treatment (Supplementary Fig. 6).
611 Embryos cultured in 50% FASW alone at 26ºC, or with the equivalent amount of DMSO, hatched
612 normally (Supplementary Fig. 6).

613

614 *Microscopy*

615 Embryos for multiview lightsheet imaging were injected at the 1-cell stage with 2 µg/µl *H2A-*
616 *mCherry* (nuclei) and *Lyn-EGFP* (membrane) mRNA reporter constructs. We mounted 4-cell
617 stage embryos inside of a 2mm PTFE tube and 3mm glass capillary suspended in 1% low melt
618 agar made in filtered ASW and infused with 500 nm fluorescent beads (F-X050, F-Y050 or F-
619 XC050 microspheres, Estapor Merck). Capillaries were mounted on a SiMView multiview
620 lightsheet microscope[103] and embryos imaged with a 488 nm (*Lyn-EGFP*) and 594 nm (*H2A-*
621 *mCherry*) laser at ten-minute intervals from three or four angles with two objectives positioned
622 180º apart. The z-interval was set to 0.41µm. The resulting six or eight views per sample were
623 registered and fused using the MultiView Reconstruction and BigDataViewer plugins for Fiji[104–]
624 [107].

625 Live imaging of *H2B-mRFPruby* transgenic embryos and *LA-mNG* or *Ph-sqh-mNG* mRNA
626 injected embryos was carried out at 26ºC on a Nikon CSU-W1 SoRa Spinning Disc confocal
627 microscope with a 20x objective. Embryos were mounted individually on glass microscope slides
628 so that a 1.5 coverslip with clay-feet spacers could be used to roll the desired region of the germ-
629 disc or grid into the field of imaging. We applied slight pressure to the coverslip to flatten the
630 tissue and obtain clearer views of apical cell face geometries. We then filled the space between the
631 coverslip and slide with FASW and sealed the edges with Vaseline to prevent evaporation. Time-
632 lapse imaging of live embryos was carried out at ten-minute intervals with a z-interval of 0.9µm.
633 Fixed and stained embryos were cleared in 70% glycerol and mounted individually in the same
634 manner as live embryos for confocal imaging on either a Nikon CSU-W1 SoRa Spinning Disc

635 (0.9µm z-interval) or Zeiss LSM 880 (1µm z-interval). Only timelapse datasets taken of embryos
636 that hatched successfully were used for analysis.
637
638 *Image analysis and segmentation*
639 Lineage tracing of the fused lightsheet datasets was performed with either semi-automated
640 (Embryo 1; Supplementary Table 1) or manual tracking (Embryos 2 and 3). The nuclear channel
641 of Embryo 1 was first pixel classified and then object tracked in ilastik[108] (ver. 1.3.3), followed by
642 manual correction in MaMuT[94] (ver. 1.53), a plugin for Fiji. Embryos 2 and 3 were tracked entirely
643 manually using both the nuclear and membrane channels in MaMuT [94] or Mastodon in Fiji. We
644 created the 2D conformal maps of the embryo's surface from the lightsheet datasets using a version
645 of ImSAnE[109] customized for *P. hawaiensis*[34]. Nuclear tracks colored according to 16-cell stage
646 lineages were superimposed onto the maps using a custom MATLAB script or manually
647 superimposed in Adobe Illustrator (CC 2023 or 2024). Maximum intensity projections of the
648 lightsheet 2D conformal maps of *Lyn-EGFP* (membrane marker) were segmented in the Fiji plugin
649 TissueAnalyzer[110] using a watershed algorithm with manual correction.
650 To visualize and quantitatively describe cell shapes, we first pixel-classified membranes in
651 10µm maximum intensity projections of Phalloidin-stained or *LA-mNG*-labeled embryos in
652 ilastik[108] (ver. 1.4.0) to generate a more consistent cell boundary signal. Especially in the later grid
653 stages (approximately 62 hpf onwards), the embryo must be carefully laid flat against the slide and
654 slightly compressed with the coverslip. For samples in which flattening out all wrinkles or
655 depressions in the tissue was not possible, the probability maps containing apical cell faces for
656 each tissue region were cut out and composited together using the Image Calculator in Fiji. We
657 then fed the probability maps exported from ilastik[108] (ver. 1.3.3) into Cellpose[111] (ver. 3.0) and

658 obtained cell ROIs using a custom-trained model with some manual correction of contiguous
659 masks. Automatic size calibration was performed and non-contiguous or incomplete cell masks
660 around the edges were removed. All subsequent quantitative descriptions of cell shape and tissue
661 organization were carried out on these ROIs using custom Python scripts available at
662 https://github.com/boyonpointe/parhyale_morpho/tree/main with commit ID a19a88d. All other
663 measurements, including intensities of cytoskeletal components, were made on 10µm maximum
664 intensity projections in Fiji (ver. 2.1.0) using the ROI section and associated measurement tools.

665 For cell shape and vertex IL measurements, each 10 µm maximum intensity projection
666 was cropped to 207 µm wide x 104 µm high. The crop box was centered on the germ disc
667 parallel to the dorso-ventral axis and centered on the midpoint of the IL (a clear straight or
668 slightly bent line) in the anterior-posterior axis. Only cells contained fully within the crop box
669 were counted.

670 For IL actin and myosin 2 measurements, in un-cropped 10 µm maximum intensity
671 projections, the lateral extent of the IL region of interest was determined by drawing a line from
672 the ventral midline of the germ disc towards the left and right sides of the germ disc. The region
673 was considered terminated when it reached cells whose sides were bent more than approximately
674 15º from the leading edge of the region. The mean IL length for phalloidin-stained samples (F-
675 actin) was 146 µm (n = 38) and the mean IL length for *Ph-sqh*-labeled samples (myosin 2) was
676 151 µm (n = 14).

677 To compare cell shape distributions in the posterior of the germ disc, we used a bootstrap
678 approach. For each pair of distributions, we generated 100,000 surrogate pairs of random
679 resampling and calculated the difference in their means. This gave us a null distribution of
680 differences, against which we assessed how often the observed empirical difference would occur.

681 The p-value corresponds to that probability. For stop motion in Movie 3, images were printed on
682 light-permeable paper and animated over a lightbox using a Sony A7S camera controlled by the
683 stop-motion animation software DragonFrame (v4).
684
685 *Cell shape descriptor*
686 To measure cell shape, we used a custom descriptor in which the area of a cell face is divided by
687 the area of the circle whose diameter is equal to the distance between the farthest two points on
688 the cell's perimeter. With this descriptor, a perfect square has a value of 0.64, and hexagons and
689 higher order polygons have values of approximately $\geqslant 0.75$. We found this measurement to more
690 usefully describe the emergence of square-cell packing than counting the number of cell sides,
691 because within this dynamic tissue, 4-way vertices frequently dissolve into small edges at square
692 corners, and cell divisions can introduce temporary kinks into neighboring cell edges.
693
694 *Cellular Potts Model Implementation*
695 Our model to test the effect of differential adhesion between different cell lineages was formulated
696 in the Cellular Potts Model (CPM)[41,67,112]. We implemented our model using Compucell3D[43]. In
697 CPM, the cells are modeled as a spatially contiguous collection of pixels. The pixels that are at the
698 boundary of cells have an energy cost associated with interacting with pixels belonging to the
699 neighboring cells. The energy cost between a pair of pixels (a,b) depends on the cell type
700 $(\sigma(a), \sigma(b))$ of both the cells to which the interacting pair of pixels belong. The area of (A) of a cell
701 is defined as the number of pixels the cell encompasses while the perimeter (L) is the number of
702 pixels at the boundary of the cell.

703 The following equation shows the expression of energy of the system for given pixel
704 configuration:

705 $$E = -\sum_{a,b} J(\sigma(a), \sigma(b)) - \sum_{\sigma} \lambda_A \left(A_\sigma - A_0(t)\right)^2 - \sum_{\sigma} \lambda_L \left(L_\sigma - L_0(t)\right)^2$$

706 The second and third terms on the right hand side of the equation represent the energy cost for cell
707 area and cell perimeter to deviate away from the steady state values A_0 and L_0 respectively. To
708 implement growth, A_0 is made a function of time such that the cell grows to reach A_0 and when it
709 meets the size to undergo division, it divides. The steady state value for the perimeter is also a
710 function of time and set to ensure that steady state shape is circular i.e. $L_0(t) = 2\pi\sqrt{A_0(t)/\pi}$. The
711 symmetric matrix J has its number of rows and columns equal to the number of cell types in the
712 system. Each entry $J_{i,j}$ in the matrix specifies the interaction energy between pixels belonging to
713 cell type i and j. In our simulation there are six different cell types corresponding to six different
714 lineages and an additional one that corresponds to the medium.

715 The segmented cell masks of tissue imaged at 26 hpf is used to generate the initial
716 configuration of the pixels in the simulation. Each pixel belongs to one among the 6 different cell
717 types or to the medium. The cells increase in size by 100 pixels before they divide. The amount of
718 growth cells undergoes before they divide is chosen to reflect the empirically observed increase in
719 tissue size and cell numbers seen at 46 hpf. The cells divide symmetrically along the axes
720 orthogonal to the major axis (long axis). Throughout the simulation, we track the number of pixels
721 in contact with pixels from cells of different lineages.

722

723 *Ablation experiments*

724 Ablation experiments were carried out on a Zeiss 980 NLO 2-photon microscope with a pulsed
725 Spectra-Physics InSight X3+ laser set to 927 μm wavelength and an ablation ROI with a 1μm

726 width that was passed over five times. *LA-mNG* embryos injected at the 1-cell stage were incubated
727 to the desired stage and mounted individually on slides with a Vaseline-sealed coverslip. Ablated
728 embryos were imaged with a LD LCI Plan-Apochromat 25x/0.8 objective for two frames prior to
729 the ablation followed by every second for two minutes immediately afterwards. Some embryos
730 were further imaged on the same microscope at intervals of one minute to follow the effects of the
731 ablation. Embryos used for further analysis were then recovered from the slide and transferred to
732 a 35mm petri dish with fresh FASW with 1:100 Penicillin-Streptomycin (10,000 U/mL penicillin,
733 10,000 µg/ml streptomycin; Gibco 15140-122) and 1:200 Amphotericin-B (250 µg/ml, Gibco
734 15290-026) for incubation at 26 ºC until fixation. Recoil length was calculated in Fiji by
735 subtracting the distance between cell vertices on either side of the ablation ROI in the first frame
736 immediately post ablation, from the distance between the same two vertices before the incision
737 was made.
738
739 *Figure presentation*
740 Line tracing of membranes shown in figures was performed using the Image Trace function
741 (Silhouettes or Line Art) on exported Cellpose[111] ROIs or on hand segmented micrographs
742 (Supplementary Fig. 3) in Adobe Illustrator 2024 or 2025. To more clearly display the
743 relationship between Engrailed expression and grid geometry in Figure 1, we used ilastik[108]
744 (ver.1.3.3) to pixel-classify images of anti-Engrailed staining and exported the resulting
745 probability maps. In Movie 4, TissueAnalyzer[113] was used to track and visualize cell membranes
746 of the midline founder population in a conformally mapped time-series that was manually
747 aligned. All figures were assembled with Adobe Illustrator.

Acknowledgements

The authors thank William Lemon and Philipp Keller (HHMI Janelia Research Campus) for providing access and training on their SimView lightsheet microscope, Sebastian Streichan and Dillon Cislo (University of California, Santa Barbara) for help with ImSAnE and applying MaMUT tracks to ImSAnE maps, John Rallis and Myrto Ziogas (IMBB-FORTH) for help with plasmid preparations, as well as members of the Extavour and Pavlopoulos laboratories for discussion.

Author Contributions

BS conceived of the study, designed experiments, performed all wet lab experiments, performed data analysis and interpretation, and wrote the first draft of the manuscript. LB designed, performed embryo collection and injection experiments for, and executed capture of lightsheet datasets, and reviewed the manuscript. CK designed and performed all computational modelling experiments, performed data analysis, and reviewed the manuscript. ES and AP conceived of the study, designed and created all fluorescent *P. hawaiensis* constructs, performed embryo collection and injection experiments for capture of lightsheet datasets, and reviewed the manuscript. CGE conceived of the study, performed data interpretation, obtained funding for the study, supervised its execution, and edited the manuscript.

Funding

This work was supported by a National Science Foundation (NSF) Graduate Student Research Fellowship 2018259071 and a Simmons Award from the Harvard Center for Biological Imaging to BLS, NSF award IOS-2220747 to CGE, the NSF-Simons Center for Mathematical and Statistical Analysis of Biology at Harvard (award number DMS-1764269) and the Harvard Quantitative Biology Initiative (CK), Human Frontiers Science Program Grant RGP022/2023 and HHMI Janelia Research Campus Visitor Program to ES and AP, and funds from the Howard Hughes Medical Institute (HHMI) and Harvard University. CGE is an HHMI Investigator.

Conflicts of Interest

The authors declare no conflicts of interest.

Data Availability

Lightsheet datasets described in Supplementary Table 1. MaMuT lineage tracks for these datasets, as well as scripts for cellular potts model simulations and image analyses, are available at https://github.com/boyonpointe/parhyale_morpho/tree/main with commit ID a19a88d.

Statement on Use of Machine Learning, Artificial Intelligence and Large Language Models

ChatGPT 4.0 and 5.0 (open AI) were used to modify R code for altering plot aesthetics. ilastik[108] and Cellpose[111], used for image segmentation in this study, are machine learning-based programs. ML/AI was not used to generate any content, write any text, or perform any other data analysis.

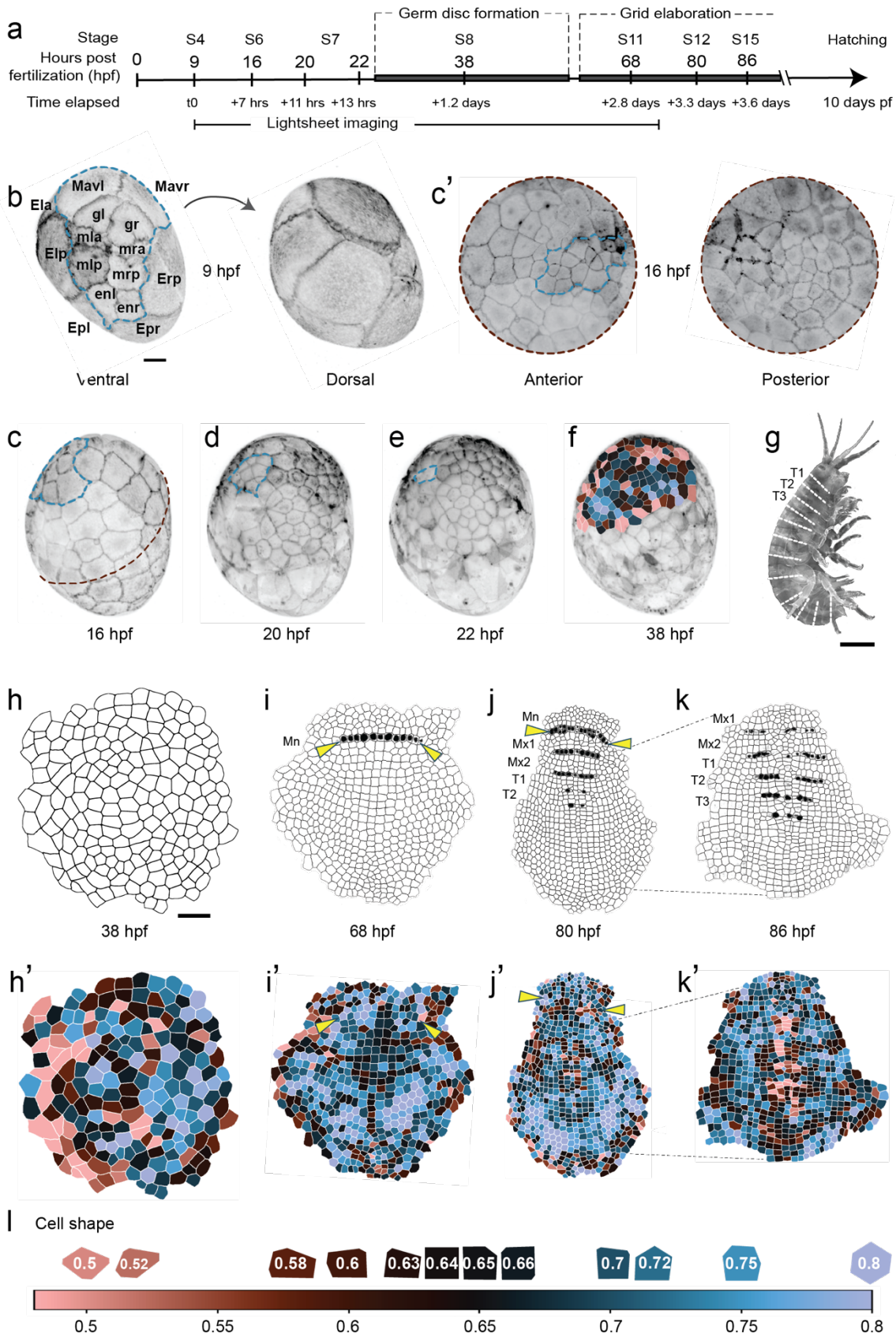
a
Germ disc formation
Grid elaboration
Stage
S4
S6
S7
S8
S11
S12
S15
Hatching
Hours post fertilization (hpf)
0
9
16
20
22
38
68
80
86
Time elapsed
t0
+7 hrs
+11 hrs
+13 hrs
+1.2 days
+2.8 days
+3.3 days
+3.6 days
10 days pf
Lightsheet imaging
b
Mavl
Mavr
Ela
gl
gr
mla
mra
Elp
mlp
mrp
Erp
enl
enr
Epl
Epr
9 hpf
Ventral
Dorsal
c'
16 hpf
Anterior
Posterior
c
d
e
f
g
T1
T2
T3
16 hpf
20 hpf
22 hpf
38 hpf
h
i
j
k
Mn
Mx1
Mx2
T1
T2
T3
38 hpf
68 hpf
80 hpf
86 hpf
h'
i'
j'
k'
l
Cell shape
0.5
0.52
0.58
0.6
0.63
0.64
0.65
0.66
0.7
0.72
0.75
0.8
0.5
0.55
0.6
0.65
0.7
0.75
0.8

Figure 1 (previous page). Formation of a cellular square grid in the *Parhyale hawaiensis* embryonic ectoderm. a Developmental timeline from fertilization to the hatching of juveniles with the window of lightsheet microscope imaging indicated at the bottom. Stages according to Browne and colleagues[29]. **b-f** Stills selected from a time-lapse of the first 1.5 days of development in a *P. hawaiensis* embryo that was live-imaged with a multiview lightsheet microscope; cell membranes marked with *Lyn-EGFP*. Micrographs are maximum intensity projections of a volume constructed by fusing 3D image stacks from all imaging angles, and are displayed either from a fixed perspective (b-f) or as conformal surface maps (c'). **b** Ventral (left) and dorsal (right) views of the 16-cell stage. The first cell divisions in *P. hawaiensis* are highly stereotypic and segregate the germ layers and germ line (gl and gr) by this stage. The eight micromeres and two macromeres enclosed within the blue dotted line are the mesoderm (ml, mr, Mav), endoderm (en), and germ-line (g) precursors, the descendants of which delaminate from the surface during gastrulation (c-e) leaving at the surface a continuous sheet of epithelial ectoderm (f). The remaining six macromeres (Epr, Epl, Era, Erp, Ela, Elp) will give rise to all ectodermal cells. **c-e** From approximately 16-22 hours post fertilization (hpf), cells begin reducing in size and migrate to the anterior pole, condensing into a germ disc (embryonic rudiment) sitting atop larger yolk-filled cells. **c'** Anterior (left) and posterior (right) conformal maps of the same image volume displayed in c. These 2D surface projections allow for simultaneous visualization of cell shapes and relationships that make up the embryo's curved surface. The maroon dotted line in c corresponds to those along map edges in c'. **f** By approximately 38 hpf, the surface of the germ disc is an epithelium made up entirely of ectoderm (colored cells). **g** An adult female *P. hawaiensis.* White lines indicate parasegmental boundaries with corresponding morphological segment identities. **h-k** Time series of fixed embryos in which the ectoderm was dissected away from the yolk and physically flattened to make surface cell geometries visible. A grid of four-sided cells emerges within the expanding germ disc. The transition from hexagonal to square cells (**h'-k'**) progresses from anterior to posterior and laterally left and right (**i**). A row of cells expressing the segmentation gene *engrailed* appears in the prospective mandibular segment (Mn) around 68 hpf (arrowheads). **j, k** From 80 hpf onwards, progressing from anterior to posterior, nuclear-localized Engrailed protein is detectable in cells of the anterior-most cell row in each parasegment as it is generated via row-duplicating cell divisions from the midline to lateral regions. Dotted lines in j indicate the region of the embryo displayed in k. **l** Cell shape descriptor used to analyze square grid morphogenesis in this study. While four-sided cells can be either square or rectangular, for simplicity we describe them as square throughout the text, and our cell shape descriptor gives square cells a metric value of 0.64. Mx1: first maxillary segment; Mx2: second maxillary segment; T1: first trunk segment; T2: second trunk segment; T3: third trunk segment.

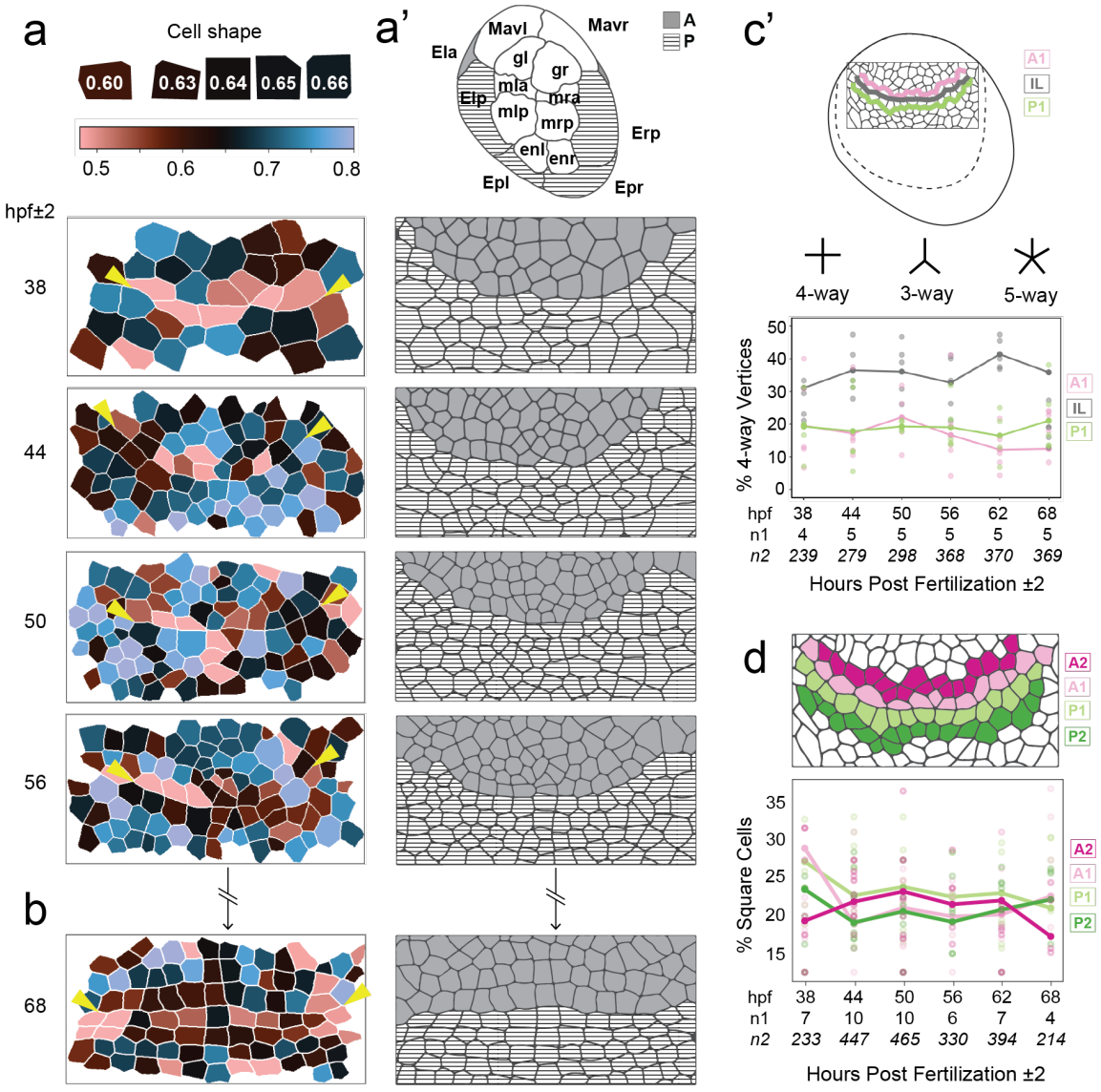

Figure 2. Square cell geometry initiates along the dorso-ventral axis at the initiation line, which is an ectodermal lineage compartment boundary. a-b 38-68±2 hpf manually flattened germ discs segmented to identify cell membranes, with cells colored according to their shape descriptor value. What we call the "initiation line" (IL; arrowheads in the left column), corresponds to the boundary of the anterior (A: grey) and posterior (P: striped) lineage compartments shown in a'. **a'** Stills from a lightsheet time-lapse that were conformally mapped onto 2D, showing descendants of ectodermal precursor macromeres (grey: anterior ectoderm founders Era, Ela; striped: posterior ectoderm founders Erp, Elp, Epr, Epl) The boundary between anterior and posterior clones begins as a jagged curve at 38±2 hpf and straightens out by 68±2 hpf. **c** Top: Schematic shows the analyzed region (box) within the germ disc (dotted line). Bottom: Percentage of 4-way vertices at the IL (gray), the equivalent line one cell anterior (A1, light pink), and one cell posterior (P1, light green). **d** Top: Cell rows analyzed in four different locations relative to the IL: immediately adjacent to the IL to the anterior (A1: light pink), immediately adjacent to the IL to the posterior (P1: light green), one cell diameter anterior to the IL (A2: dark pink) and one cell diameter posterior to the IL (P2: dark green). Bottom: plot showing percentage of square cells (shape descriptor value ⩾ 0.60 or ⩽0.66). Anterior is up in all images. Sample sizes in c and d indicated by n1: number of embryos and n2: number of vertices.

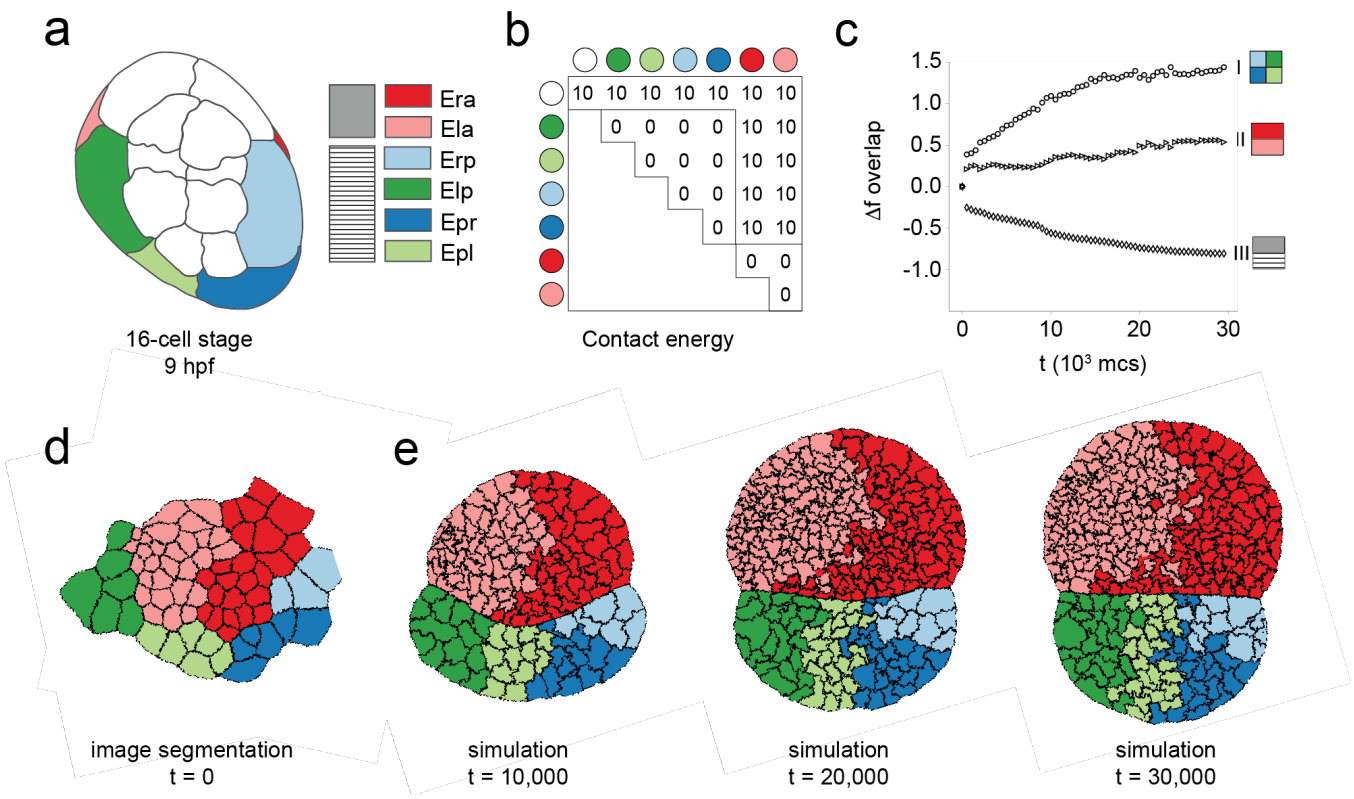

Figure 3. A simulation of cell sorting can explain the emergence of a straight boundary at the initiation line. a Tracing of a 16-cell stage embryo with the six ectodermal lineages colored. Grey and striped legend is provided to show the correspondence of these blastomere lineages to the anterior and posterior compartments shown in Figure 2. **b** Simulation contact energy inputs for each combination of lineage precursors (colored circles show blastomere identities as defined in a) as well as the environment surrounding the tissue (white circles). Higher contact energy results in decreased affinity between cells. **c** Change in normalized area of overlap plotted against time in Monte Carlo steps (mcs) for n = 10 runs of the simulation. Group I (circles) = boundaries among the four posterior lineages (Erp, Elp, Epr, Epl); group II (triangles) = boundary between the two anterior lineages (Era, Ela); group III (diamonds) = boundary between the anterior and posterior lineages. **d** Membrane segmentation of part of the conformally mapped germ disc of Embryo 1 (Supplementary Table 1) at 26 hpf. At this stage, gastrulation has already taken place, and the surface of the embryo is a continuous sheet of ectoderm. This segmentation was seeded as the starting point for the simulation. **e** Stills from three time points of the simulation of cell sorting among the 16-cell stage ectodermal lineages implemented in CompuCell3D with time denoted in arbitrary units. Cell division rates for each lineage from one of the lightsheet datasets were input into the model. Anterior is up in all embryo image panels.

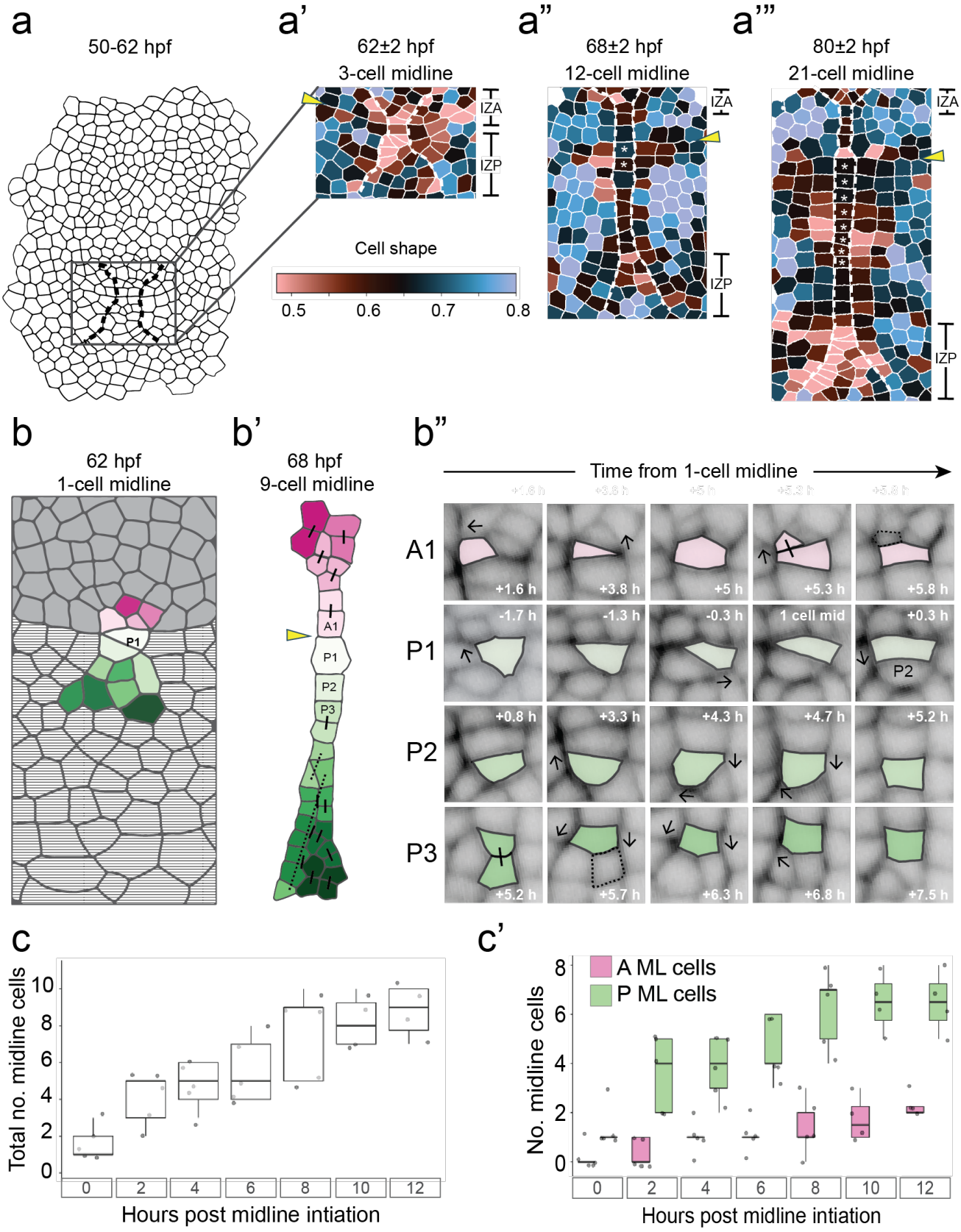
a
50-62 hpf
a'
62±2 hpf
3-cell midline
a"
68±2 hpf
12-cell midline
a'''
80±2 hpf
21-cell midline
IZA
IZP
Cell shape
0.5
0.6
0.7
0.8
b
62 hpf
1-cell midline
P1
b'
68 hpf
9-cell midline
A1
P1
P2
P3
b"
Time from 1-cell midline
A1
P1
P2
P3
+1.6 h
+3.8 h
+5 h
+5.3 h
+5.8 h
-1.7 h
-1.3 h
-0.3 h
1 cell mid
+0.3 h
+0.8 h
+3.3 h
+4.3 h
+4.7 h
+5.2 h
+5.7 h
+6.3 h
+6.8 h
+7.5 h
c
Total no. midline cells
Hours post midline intiation
c'
A ML cells
P ML cells
No. midline cells
Hours post midline intiation

852

853 **Figure 4 (previous page). The secondary grid axis emerges as a column of square cells via the**
854 **intercalation of a polyclonal founder cell population. a** At 52-62 hpf, primarily anisotropic ectodermal
855 cells near the ventral midline and spanning the IL (arrowheads in a', a", a'"), in a region we denote the
856 intercalation zone (IZ), intercalate simultaneously in the anterior and posterior directions to form a single
857 column of square cells forming the midline of the embryo (**a'**). **a"** The cells within the midline are the first
858 cells to become square. Cells flanking the midline on the left and right then adopt square shapes posterior
859 to the IL. Cells in a', a", and a'" are colored according to the cell shape descriptor. * in a" and a"' indicates
860 midline cells that have undergone parasegment precursor row duplication. **b** Cells that join the midline
861 derive from a polyclone of founder cells that span the anterior (grey)-posterior (stripes) compartment
862 boundary (arrowhead). **b'** Founder cells intercalate in both anterior (IZA) and posterior (IZP) intercalation
863 zones (as shown in a', a" and a'"), adding or subtracting sides until they form a square. Arrows indicate the
864 direction of a growing or shrinking cell side. Dotted outlines in rightmost panel of top row and second panel
865 of bottom row indicate the outlines of the sister cell resulting from the division in the previous panel. **c**
866 Numbers of total cells in the midline over time (n = 5 embryos). Midline initiation is defined as the time
867 when the first posterior cell (P1) is aligned. By 12 hours after midline initiation, a mean of nine total cells
868 have been added to the midline. **c'** Numbers of cells in the midline anterior (A ML: pink) and posterior (P
869 ML: green) to the IL over time (in = 5 embryos). Anterior is up in a-a"' and b-b''.

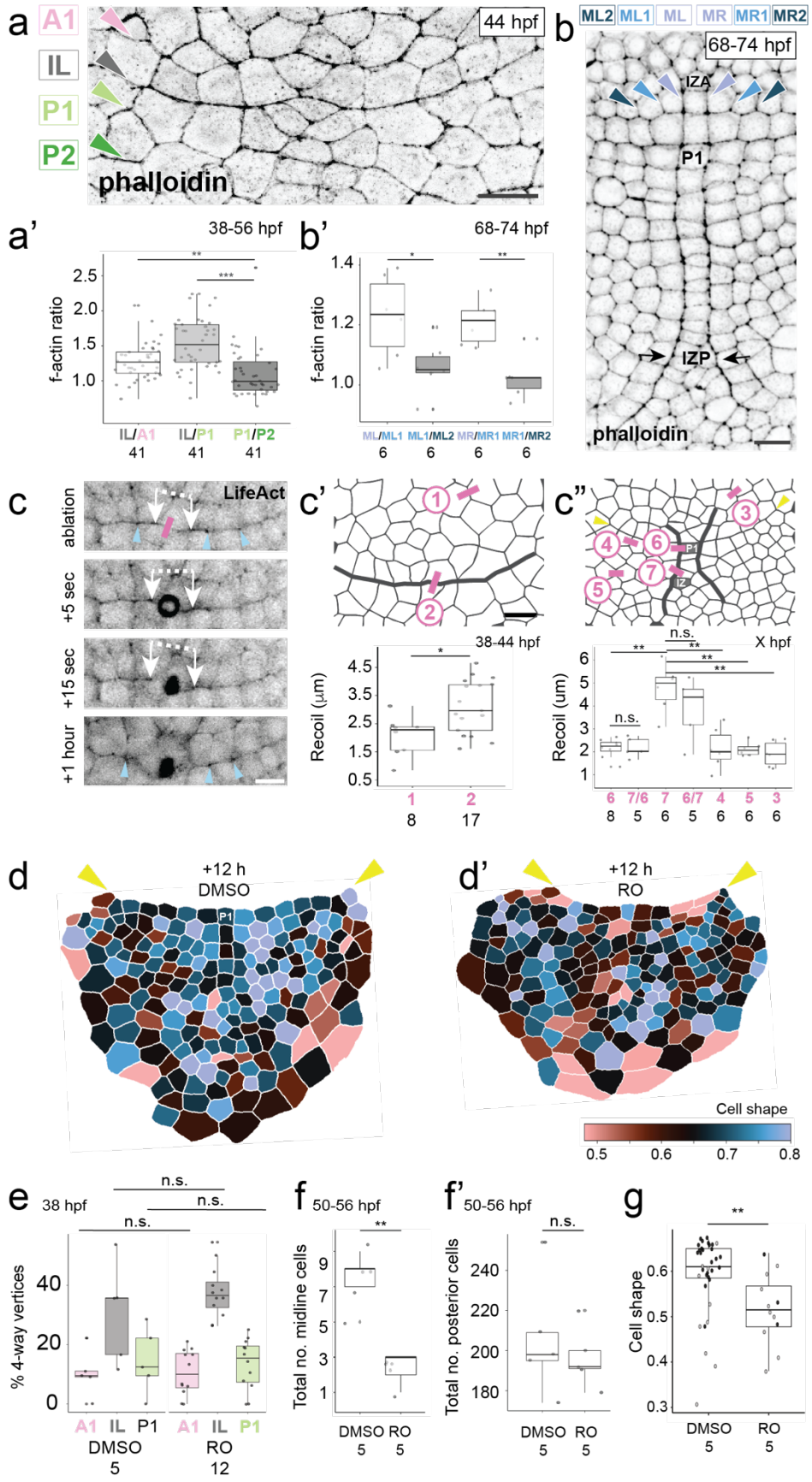
a
A1
IL
P1
P2
44 hpf
phalloidin
b
ML2 ML1 ML MR MR1 MR2
68-74 hpf
IZA
P1
IZP
phalloidin
a'
38-56 hpf
f-actin ratio
IL/A1 IL/P1 P1/P2
41 41 41
b'
68-74 hpf
f-actin ratio
ML/ML1 ML1/ML2 MR/MR1 MR1/MR2
6 6 6 6
c
LifeAct
ablation
+5 sec
+15 sec
+1 hour
c'
38-44 hpf
Recoil (μm)
1 2
8 17
c''
X hpf
n.s.
Recoil (um)
6 7/6 7 6/7 4 5 3
8 5 6 5 6 6 6
d
+12 h
DMSO
P1
d'
+12 h
RO
Cell shape
0.5 0.6 0.7 0.8
e
38 hpf
n.s.
% 4-way vertices
A1 IL P1 A1 IL P1
DMSO RO
5 12
f
50-56 hpf
Total no. midline cells
DMSO RO
5 5
f'
50-56 hpf
n.s.
Total no. posterior cells
DMSO RO
5 5
g
Cell shape
DMSO RO
5 5

870

Figure 5 (previous page). The initiation line and midline borders are tensile cytoskeletal cables. a Maximum intensity projection of 20 0.5µm optical sections of the ventral ectoderm of a 44±2 hpf embryo stained with phalloidin to label F-actin. **a'** Ratios of mean F-actin intensity measured in 38-56 hpf embryos. The regions quantified (A1, IL, P1, P2) are shown in **a**. Each region begins at the arrowhead on the right of the micrograph and extends across approximately 10 contiguous cell sides to the left side of the micrograph. **b** Maximum intensity projection of six 0.9µm optical sections of a 68-74 hpf embryo with a 15-cell midline; F-actin is labeled with phalloidin as in a. Arrowheads indicate the six regions (lines running parallel to the anterior-posterior axis, named MR, MR1, MR2, ML, ML1, ML2) where F-actin intensity was quantified. Each region quantified begins at the arrowhead shown in **b** and extends towards the posterior along contiguous cell sides to the posterior IZ (black arrows). **b'** Ratios of mean F-actin intensity measured in 68-74 hpf embryos with 7-15-cells in the midline. **c** 38-44 hpf embryo subject to laser ablation at the IL. **c** Pink rectangle indicates the ablation site; white arrows connected by a dashed line indicate the lengths measured to calculate recoil; blue arrowheads at IL indicate vertices surrounding the incision site. **c'** Ablation sites (top: thick line indicates the IL) and recoil plot (bottom) in 38-44 hpf embryos in which recoil was measured following IL ablation. **c"** Ablation sites (top: thick lines indicate the cables demarcating the nascent midline) and recoil plot (bottom) in 58-69 hpf embryos with 3-7 cells in the midline. Pink numbers on X-axis categories indicate the ablation site as shown in the schematic above. 7/6 indicates that a first incision was made at position 6 (next to the midline P1 cell/at the compartment boundary), followed by a second incision at position 7 (posterior IZ). In 6/7, the same two incisions were made in reverse order. **d** 1-cell midline embryos (50-56 hpf) were incubated in 50µM DMSO or Rockout (**d'**), and the cells of the posterior compartment were segmented and their cell shape descriptor was color-mapped 12 hours later. The IL is indicated by yellow arrowheads. **e** Percentage of 4-way vertices in 38 hpf embryos incubated in DMSO and 50µM Rockout for 12 hours. P-values for comparisons between DMSO and RO-treated samples as follows: A1: 0.48; IL: 0.18; P1: 0.48. **f** Total number of midline cells is significantly decreased in 62-68 hpf embryos treated with Rockout for 12 hours (p-value = 0.004). **f'** Total number of cells in the posterior compartment of 62-68 hpf embryos treated with Rockout for 12 hours is not significantly different from DMSO controls (p-value = 0.35). **g** Cell shape values for cells aligned into the midline in 12-hour DMSO (n = 35 cells) and Rockout (n = 12 cells) treated embryos. Grey symbols indicate the single cells at the anterior-most and posterior-most positions of the midline; black symbols indicate all other midline cells. Samples are the same as those plotted in f and f' (p-value = 0.002). * p-value < 0.05; ** p-value < 0.01; *** p-value < 0.001; n.s. not significant (Mann Whitney U-test; all tests one-tailed). Scale bars for a, c', d = 25µm and c = 15µm. Anterior is up in all micrographs. Sample sizes (number of embryos) in all plots indicated by numbers underneath category labels.

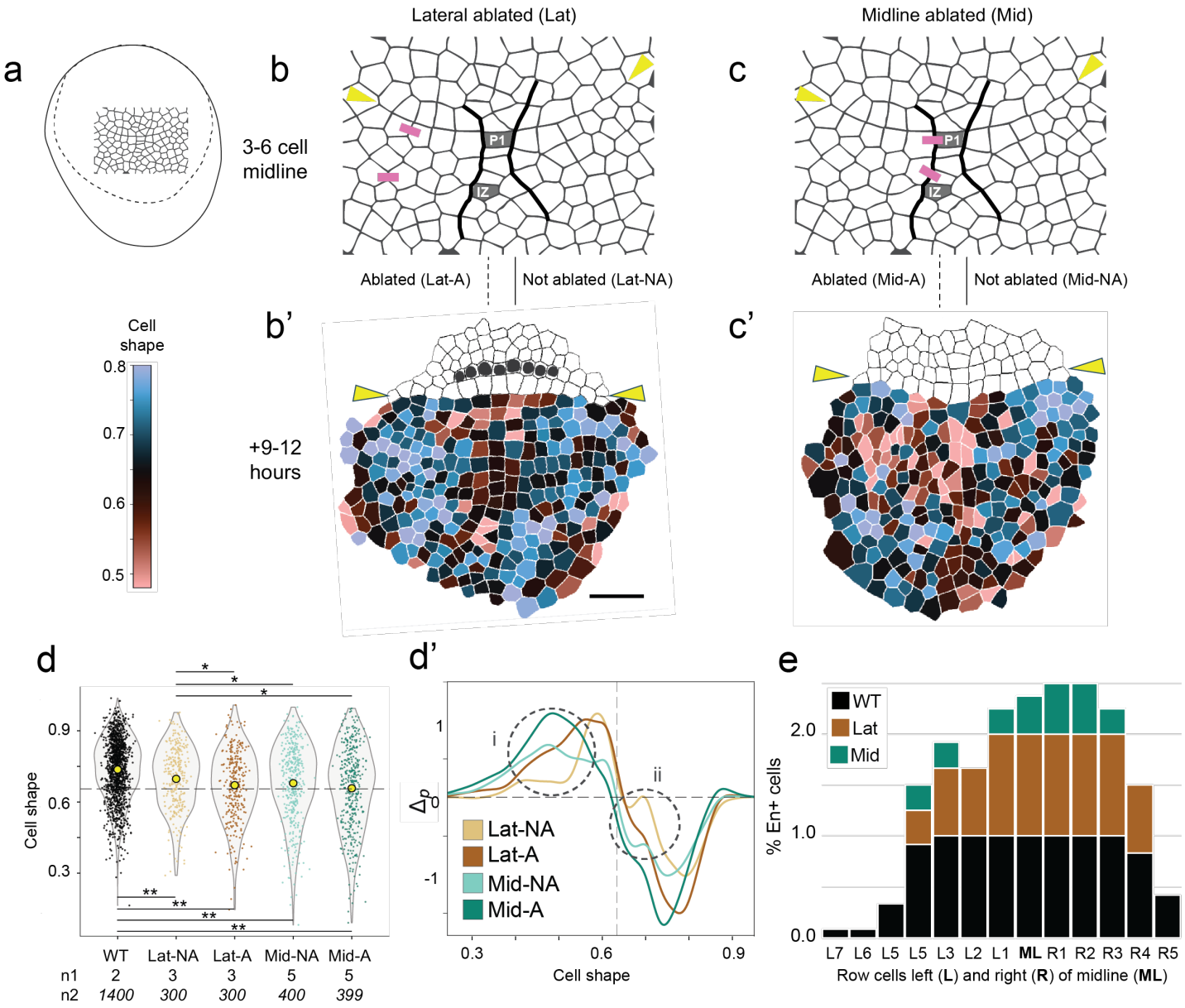
a
b
Lateral ablated (Lat)
3-6 cell midline
P1
IZ
Ablated (Lat-A)
Not ablated (Lat-NA)
c
Midline ablated (Mid)
Ablated (Mid-A)
Not ablated (Mid-NA)
Cell shape
0.8
0.7
0.6
0.5
b'
+9-12 hours
c'
d
Cell shape
WT
Lat-NA
Lat-A
Mid-NA
Mid-A
n1 2 3 3 5 5
n2 1400 300 300 400 399
d'
Δp
i
ii
Lat-NA
Lat-A
Mid-NA
Mid-A
Cell shape
e
WT
Lat
Mid
% En+ cells
L7 L6 L5 L5 L3 L2 L1 ML R1 R2 R3 R4 R5
Row cells left (L) and right (R) of midline (ML)

904

Figure 6 (previous page). The midline cables organize square-cell packing and the emergence of the first complete stripe of Engrailed-positive nuclei. a The region within the germ disc where ablations were made, delineated by the dotted line. **b, c** Locations of laser ablations performed in different regions of the ventral epithelium in 58-69 hpf embryos with 3 – 6 cells in the midline. **b', c'** Cell shape descriptor values and En expression 9-12 hours after ablation. **d** Cell shape descriptor value distributions across treatments, including unablated embryos (WT) of equivalent chronological age. Yellow circles indicate the mean, dotted line the value for an isometric square. Only significantly different pairwise comparisons (based on the bootstrapping approach described in Methods) are indicated as follows: * $p < 0.05$; ** $p < 0.01$. Sample sizes indicated by n1: number of embryos and n2: number of cells. **d'** Deviation of the four ablated groups from the WT probability density ($\Delta_p = 0$) over the range of cell shape values observed. A positive value indicates shapes gained and a negative value indicates shapes lost. Dotted vertical line indicates the value for an isometric square; colors are the same as in panel d. **e** Proportion of Mn cells (categories on horizontal axis) expressing En in wild type and in embryos subjected to lateral (brown) or midline (green) ablations shown in b and c respectively. Data in Supplemental Table 3.

Movie Legends [Download Link]

All movies show Embryo 1 (see Supplementary Table 1).

Movie 1. **The first 2.5 days of development of a membrane-labeled *P. hawaiensis* embryo**. Timelapse animation of the *Lyn-EGFP* (membrane) channel of a reconstructed multiview lightsheet dataset beginning at the 8-cell stage and ending during germ band grid elaboration. Each frame is a maximum intensity projection through half of the embryo and was taken ten minutes apart. 319 total frames are animated at a frame-rate of nine frames per second. Sequential frames from this animation were selected for and sequentially displayed in Figure 1 (first frame is Fig. 1b).

Movie 2. **The first 2.5 days of development of a nuclear-labeled *P. hawaiensis* embryo**. Timelapse animation of the *H2A-mCherry* (nuclei) channel of the same embryo shown in Movie 1. Each frame is a maximum intensity projection through half of the embryo and was taken ten minutes apart. 319 total frames are animated at a frame-rate of nine frames per second.

Movie 3. **Dynamics of the 16-cell stage lineage domains visualized by stop-motion animation**. The left side of this animation shows a still from Movie 1 with the *Lyn-EGPF* marked 16-cell stage ectodermal blastomeres false colored (Era = magenta, Ela = pink, Erp = yellow, Elp = purple, Erp = cyan, Elp = orange). The right side shows 2D maps of the same dataset in which the MaMuT nuclear tracks have been superimposed on the membrane channel to show the lineage of each cell. The rectangular cut-out corresponds to the cropped regions of each map shown in Fig. 2c, Fig. 6a, Supplementary Fig. 1 and Supplementary Fig. 8a. The maps shown here begin at 42 hpf and end at 55.67 hpf and are animated at a frame rate of nine frames per second, displaying 1.5 hours of developmental time every second. Given that the mapping of the 3D surface to 2D was not constrained and the germ disc migrates across the yolk, frames were manually aligned to produce animated motion and keep the emerging grid fixed within the cut-out region. The first sweep of the pointing finger across the map (00:07) indicates the IL (Fig. 2) at the anterior-posterior compartment boundary. The second sweep at the end (00:10) indicates the emerging midline (Fig. 4), which separates the Erp and Elp lineages by one cell beginning just posterior to the IL (P1 in Fig. 4b).

Movie 4. Intercalation of midline cells to form a column of square cells. The midline of the germ band grid forms as a single column of cells via intercalation. Cells aligned into the midline and within the intercalation zone at 66±2 hpf were tracked backwards to the onset of midline formation.

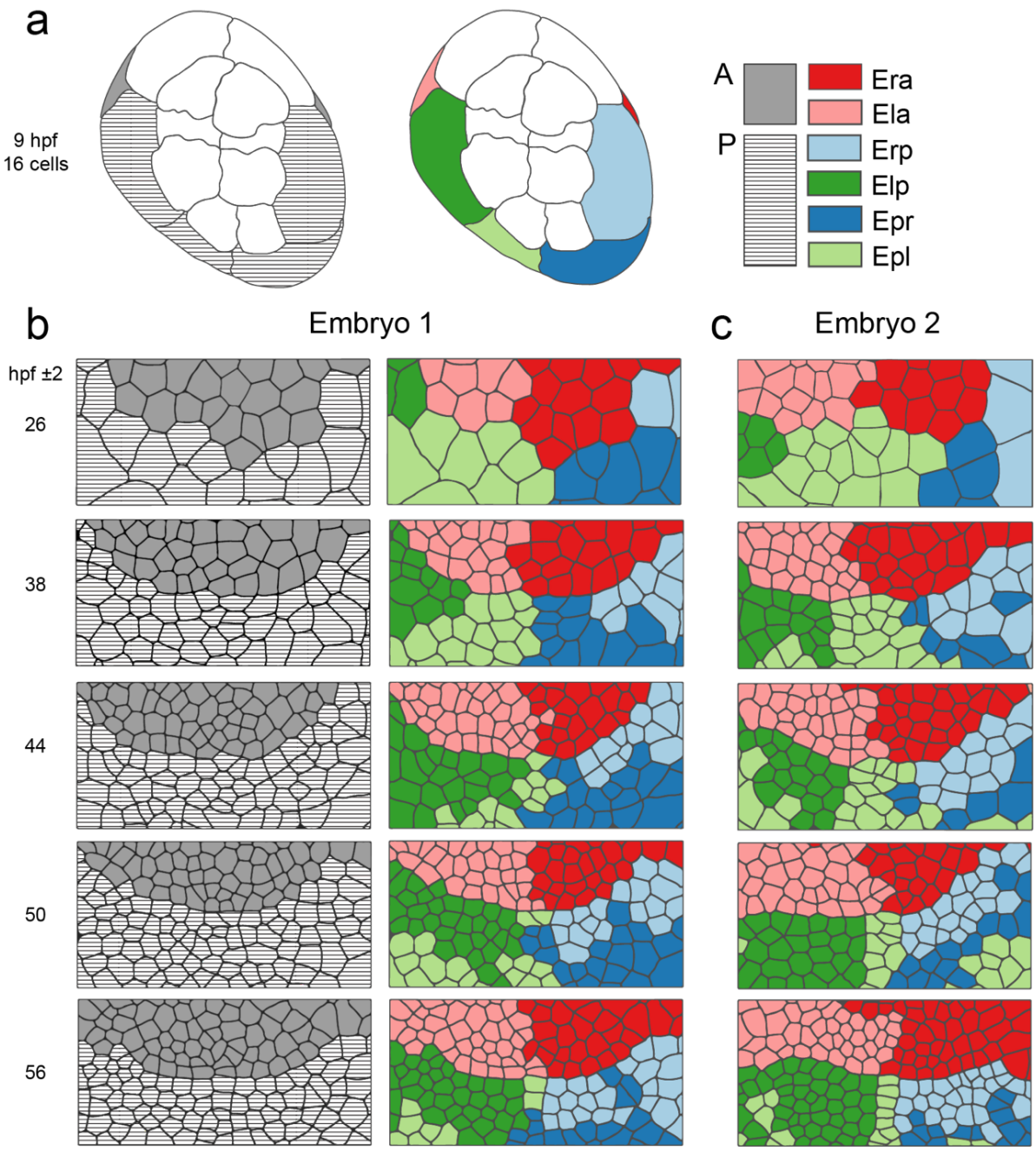

Supplementary Figure 1. 16-cell ectodermal lineage domains undergo extensive rearrangement. Stills from long-term multiview lightsheet timelapses shown either as tracings of maximum intensity projections (a) or 2D conformal maps (b-c) in which lineage was determined by tracking each cell back to its 16-cell stage ancestor. **a** 16-cell ectoderm precursor blastomere identities for Embryo 1 (Supplementary Table 1) colored with reference to anterior (grey)-posterior (striped) compartments or 16-cell stage identity (colors). **b-c** Lineage domain comparison between Embryo 1 and Embryo 2 (Supplementary Table 1) showing that in both embryos, anterior lineages (Era, Ela) do not mix with posterior lineages (Erp, Elp Epr, Epl). In the posterior compartment, the Erp and Elp domains begin on opposite (left and right) sides of the germ disc at 26±2 hpf and migrate closer to one another until they are separated by only a single column of Epr or Epl cells by 56±2 hpf, indicating the presence of extensive cell rearrangement.

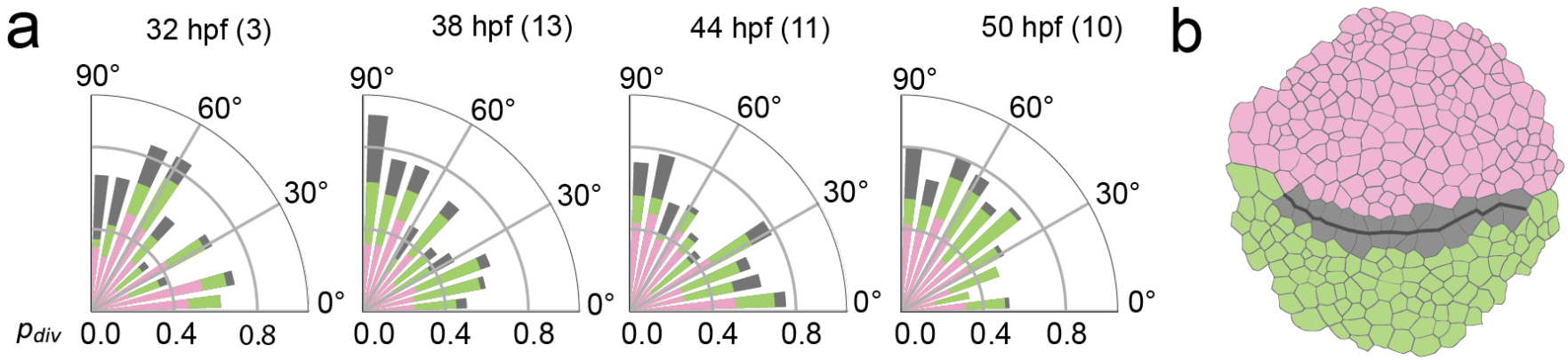

Supplementary Figure 2. Cell proliferation occurs throughout the germ disc from 32-30 hpf, with IL-adjacent divisions oriented preferentially perpendicular to the IL. a Cell division angles measured across the germ disc in 32-50 hpf embryos (sample size in parentheses). Angles are plotted with reference to the orientation of the IL (0°) and colored according to the division region (anterior = pink, IL = grey, posterior = green). **b** Segmented germ disc indicating locations of defined tissue regions. IL cell divisions are those that occur in cells directly adjacent to the IL on the anterior or posterior side (grey).

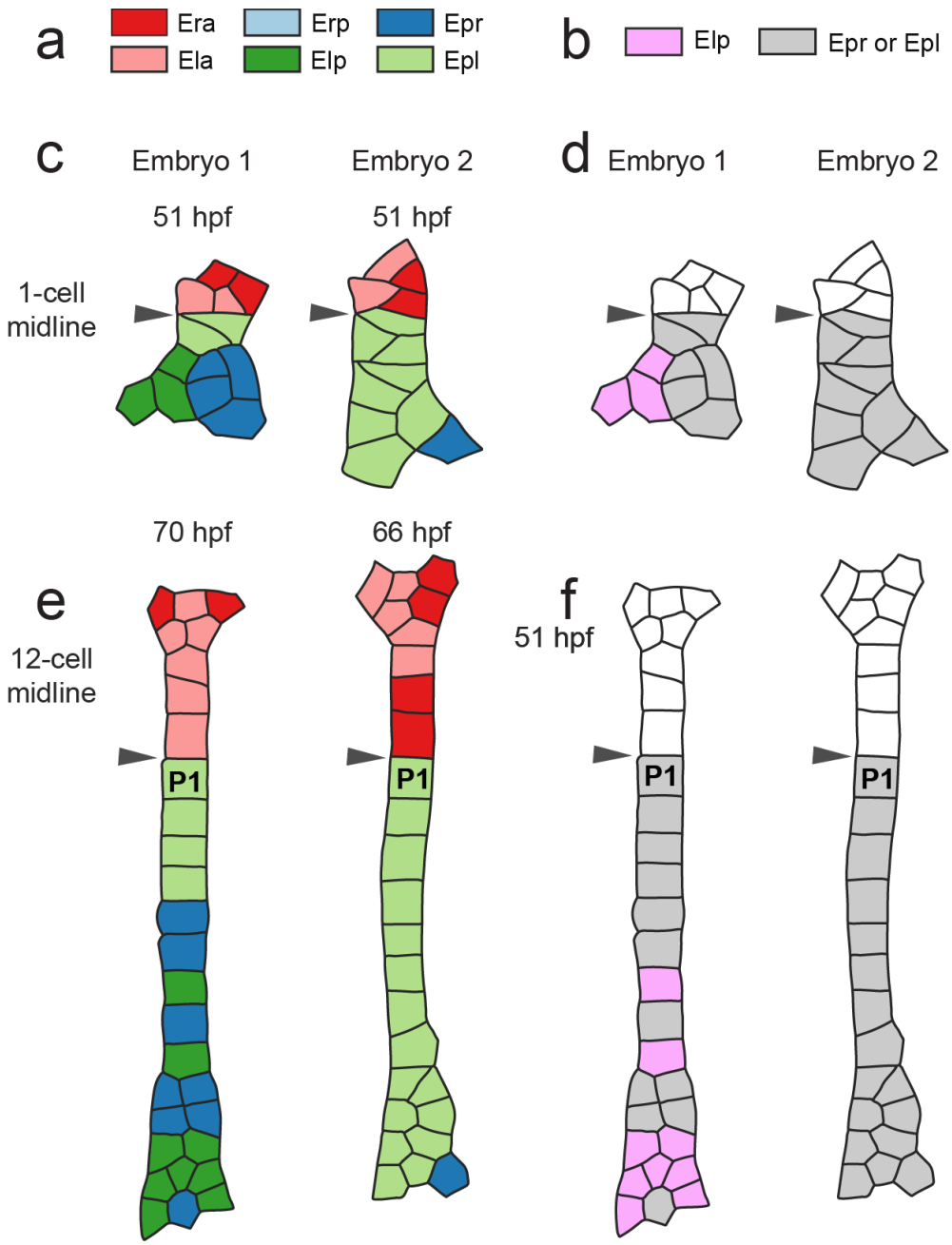

Supplementary Figure 3. Multiple 16-cell stage ectodermal lineages contribute to the midline, including non-Ep clones in the posterior. a Legend for 16-cell stage ectodermal precursor blastomeres. Midline descendants shown in c and e. **b** Legend for 16-cell stage Ep and non-Ep ectodermal precursor blastomeres. **c, e** The midline is composed of descendants of multiple 16-cell blastomeres both anterior and posterior to the anterior-posterior compartment boundary, which we call the IL at earlier stages. Midline cells in 12-cell midline embryos were tracked back to the 16-cell stage in the lightsheet datasets. At the 1-cell midline timepoint, only cells whose descendants make up the midline or intercalation zones shown in the 12-cell midline timepoints, are shown. **d, f** The posterior midline is not exclusively made up of descendants of Ep. Arrowheads indicate the location of the compartment boundary. In c through f, Embryos 1 and 2 correspond to the same datasets shown in Supplementary Figure 1 and described in Supplementary Table 1.

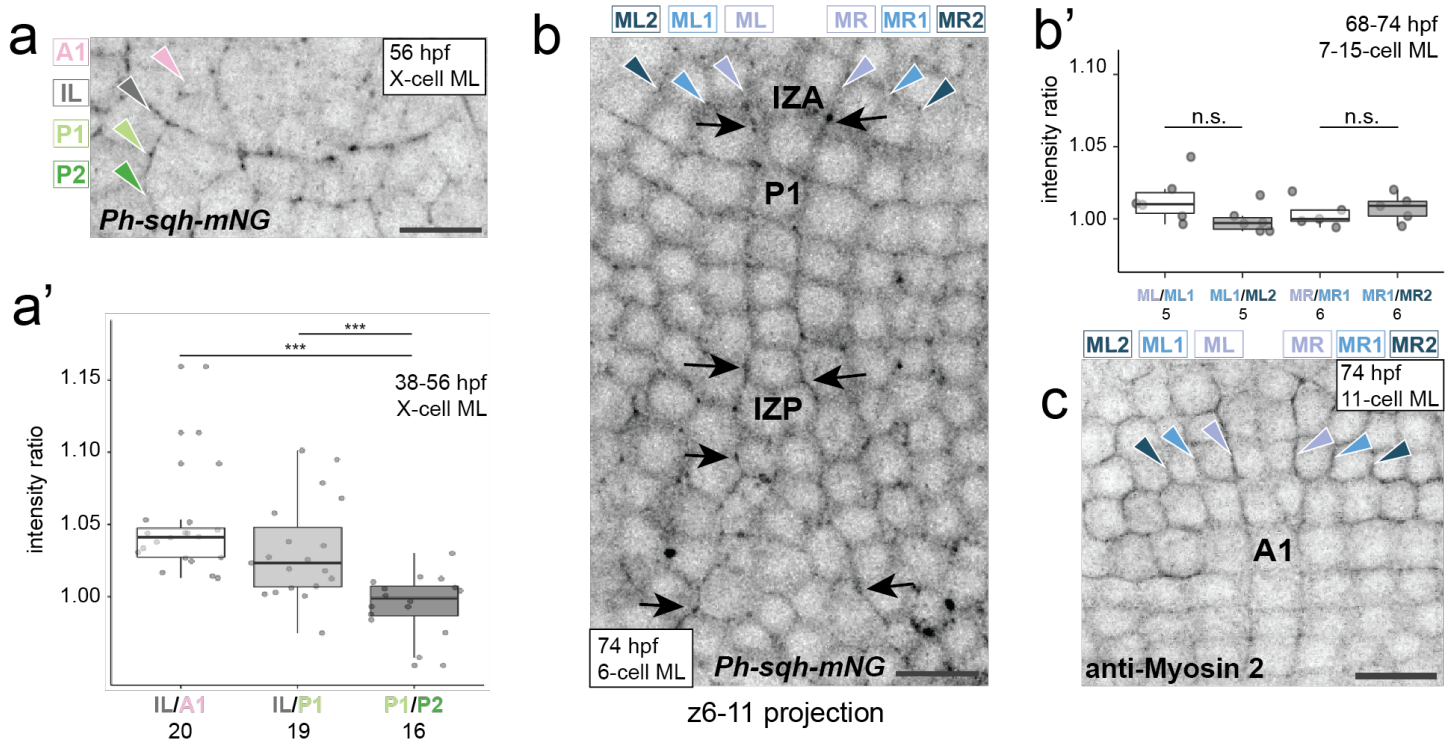

Supplementary Figure 4. Myosin 2 accumulates at the IL and midline cables. a 10µm maximum intensity projection of a 56±2 hpf embryo injected with *Ph-sqh-mNG* mRNA to label the myosin 2I regulatory light chain. **a'** Ratios of mean intensity of *Ph-sqh-mNG* signal measured from 38-56 hpf embryos in 10µm maximum intensity projections like that shown in a. The regions where *Ph-sqh* signal was quantified (A1, IL, P1, P2) are shown in a; each begins at the arrowhead and extends across contiguous cell sides to the rightmost edge of the region shown. **b** Maximum intensity projection through 5µm of a 74 hpf embryo at the 6-cell midline stage. Arrows indicate regions of myosin- 2 accumulation along the MR and ML cables (arrowheads), and at the anterior and posterior intercalation zones (IZ). **b'** Ratios of mean intensity of *Ph-sqh-mNG* signal measured from 5µm maximum intensity projections labeled with *Ph-sqh-mNG* expression . The regions quantified (MR, MR1, MR2, ML, ML1, ML2) are shown in b; each begins at the arrowhead and extends down contiguous cell sides to the bottom of the region shown. p = 0.05 for ML/ML1 compared to ML1/ML2; p = 0.20 for MR/MR1 compared to MR1/MR2. **c** 5µm maximum intensity projections of a 74 hpf embryo with 11 cells at the midline, labeled with an anti-Myosin 2 antibody. Only the anterior portion of the midline is shown here. Scale bars = 25µm and anterior is up in all micrographs. For all statistical comparisons * p-value < 0.05, ** p-value < 0.01, *** p-value < 0.001, and n.s. = not significant (Student's t-test for a; Mann Whitney U-test for b; all tests one-tailed). Sample sizes in a' and b' (numbers of embryos) indicated by numbers under category labels.

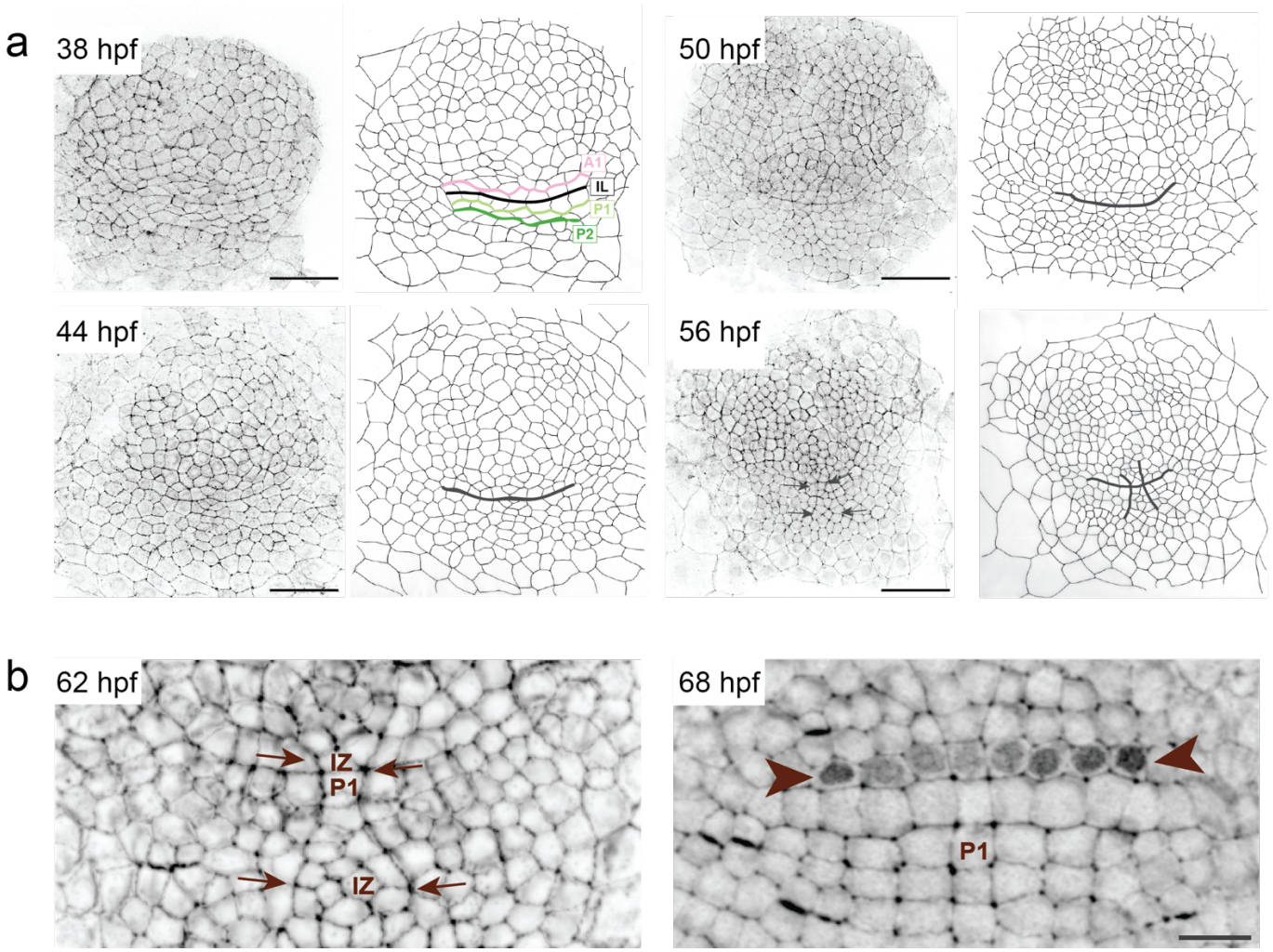

Supplementary Figure 5. IL and midline cables in the context of the whole germ disc. a 10µm maximum intensity projections of 38-56±2 hpf embryos stained with phalloidin (left) and with membranes traced (right). IL (all stages shown) and midline cables (56 hpf only) demarcated with thick lines. Anterior is up; scale bar = 100µm. **b** 10µm maximum intensity projections of the regions around the IL and midline cables in 62-68±2 hpf embryos. Arrows indicate the midline cables flanking the intercalation zone (IZ). Arrowheads indicate Engrailed expression in the prospective mandibular segment (Mn). Anterior is up; scale bar = 20µm.

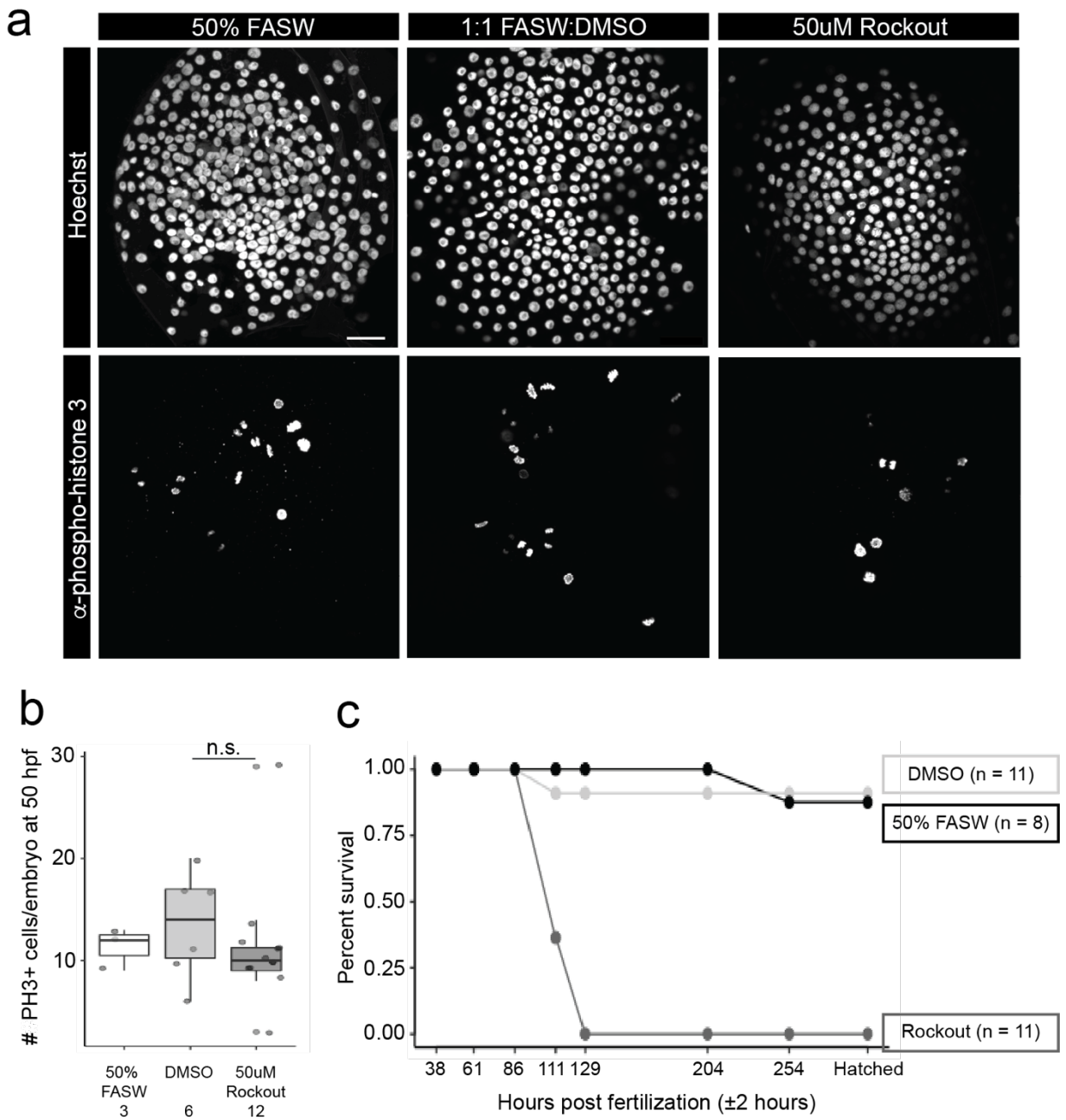

Supplementary Figure 6. 12-hour Rockout treatment does not impact cell proliferation. a 38±2 hpf embryos treated with either 50% FASW, 1:1 FASW:DMSO, or 50µM Rockout in 50% FASW were fixed 12 hours later (at 50±2 hpf), stained with Hoechst 33342 (top row) and anti-phospho-histone H3 (bottom row). Scale bar = 100µm and applies to all panels. **b** Total number of phospho-histone H3-positive cells for each treatment shown in a. n.s. = not significant (p-value = 0.303, two-tailed Mann-Whitney U Test). **c** Continuous treatment hatching assay. 100% of embryos incubated in 50µM Rockout continuously beginning at 38±2 hpf remained alive after 48 hours of treatment (86±2 hpf), and all died by 91 hours of treatment (129±2 hpf) (n = 11 embryos). By contrast, 100% of embryos in the 50% FASW (n = 8) and 1:1 FASW:DMSO (n = 11) treatments remained alive until 204±2 hpf. 87.5% hatched in 50% FASW and 90.1% of embryos hatched in 1:1 FASW:DMSO. Sample sizes in b indicated by numbers underneath category labels.

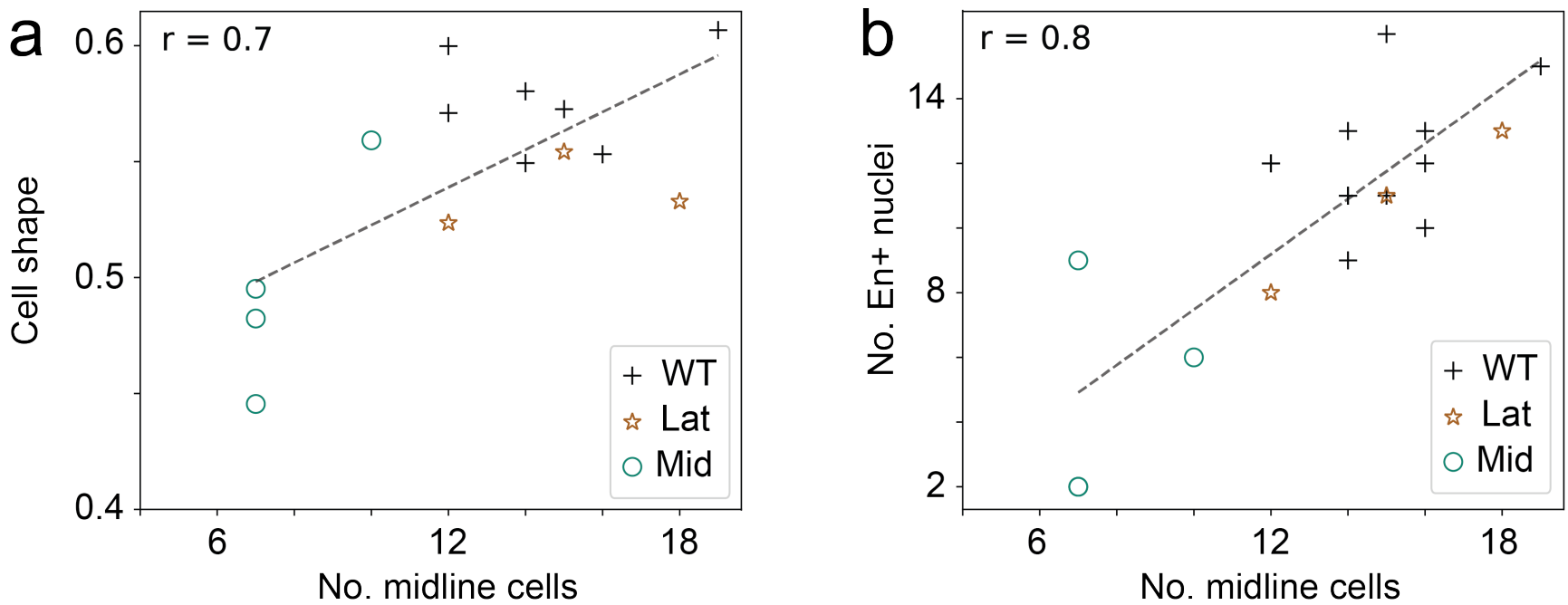

Supplementary Figure 7. a The bottom tenth percentile of the cell shape value (Fig. 1l) distribution of the whole tissue (i.e. the most anisotropic/least round cells) correlates positively with the total number of midline cells for that sample, in both wild type and ablated embryos. For wild type embryos, the roundness value of the bottom tenth percentile of cells is close to 0.6, implying that the shape of most non-round cells in wild type tissues is a square. However, upon midline ablation, the roundness value for this bottom tenth percentile is well below 0.6, implying that cells that would have been square in the wild type adopt more asymmetric shapes. The most dramatic impact on cell shape is experienced by the cells in the midline, which are approximately 10% of the cells in the tissue at this stage (data not shown). **b** The total number of Engrailed-positive (En+) nuclei correlates positively with the total number of midline cells.

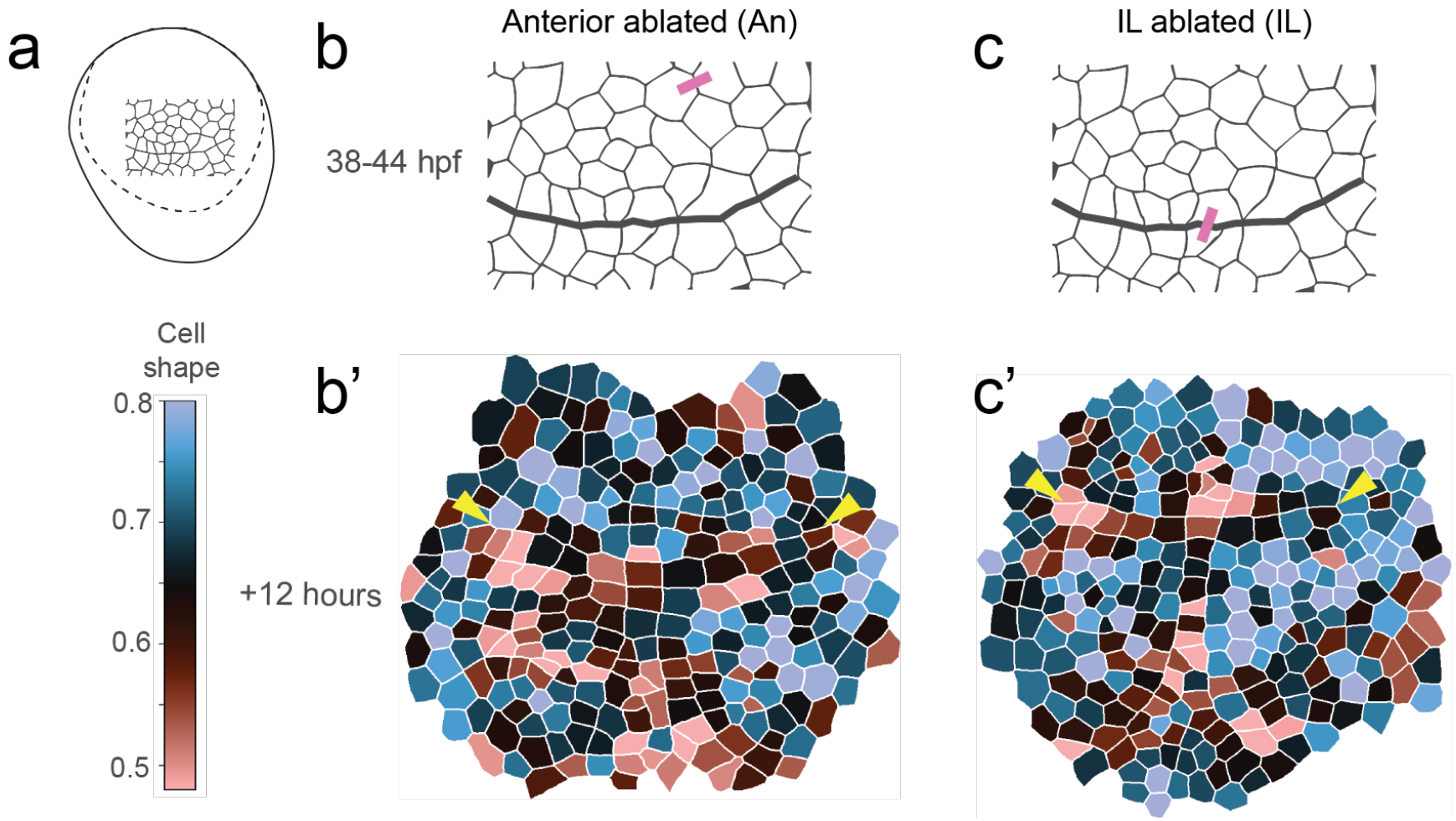

Supplementary Figure 8. Ablated IL embryos maintain a straight line at the IL and form a midline. a Schematic showing the location of the region delineated in b and c. **b** Ablation of a cell bond four cells anterior to the IL (n = 2). Ablation sites indicated by the pink rectangles. **b'** Cell shape descriptor values mapped on to +12 hour ablation tissue segmentations. **c** Ablation of a cell bond at the IL (n = 5). Ablation site indicated by the pink rectangle. **c'** Cell shape descriptor values mapped as described in b'. Arrowheads: IL.

1045

Lightsheet Sample	Total imaging time (h)	T-interval (min)	16-cell lineages tracking	Midline tracking	Posterior cell numbers	Cell division orientation	Tissue morphology seeds for simulation
Embryo 1	61.00	10	Yes	Yes	Yes	Yes	Yes
Embryo 2	61.00	10	Yes	Yes	Yes	Yes	No
Embryo 3	66.33	10	No	Yes	Yes	Yes	No
Figure			**Fig. 2, Supp. Fig. 1**	**Fig. 4, Supp. Fig. 2**	**Fig. 5**	**Supp. Fig. 3**	**Fig. 3**

1046

1047 **Supplementary Table 1. Lightsheet datasets used for analyses.** h: hours. min: minutes.

1048

					Live: 6hr time window				Fixed							
					Cell divisions in germ disc				Cell divisions in germ disc				Total cells in germ disc			
hpf	**N (live)**	**N (fixed)**	**N (total)**		**Total**	**A**	**IL**	**P**	**Total**	**A**	**IL**	**P**	**Total**	**A**	**IL**	**P**
32	3	0	3	Mean	54.33	31.33	9.67	13.33	4.67	3.33	1.33	0.00	154.00	84.00	16.67	53.33
				SD	17.16	14.05	4.04	1.53	1.53	2.31	1.53	0.00	18.19	14.93	1.15	13.65
				SE	9.91	8.11	2.33	0.88	0.88	1.33	0.88	0.00	10.50	8.62	0.67	7.88
38	3	10	13	Mean	69.33	30.33	13.00	26.00	5.42	2.67	1.00	1.92	238.92	155.33	20.62	64.31
				SD	8.50	5.13	4.58	1.73	2.11	1.61	1.00	1.04	23.60	20.72	2.10	7.97
				SE	2.36	1.42	1.27	0.48	0.58	0.45	0.28	0.29	6.55	5.75	0.58	2.21
				A vs P					0.10565				**<0.00001**			
44	2	10	12	Mean	108.50	66.00	16.00	26.50	5.45	2.91	0.75	1.75	311.91	183.64	24.33	103.83
				SD	21.92	7.07	8.49	6.36	2.62	2.07	0.75	1.36	31.23	19.30	2.57	25.56
				SE	6.33	2.04	2.45	1.84	0.76	0.60	0.22	0.39	9.02	5.57	0.74	7.38
				A vs P					0.09342				**0.00006**			
50	2	9	11	Mean	141.00	79.00	15.50	46.50	5.33	3.33	0.36	1.67	356.22	211.11	24.82	120.11
				SD	22.63	18.38	0.71	4.95	2.45	1.87	0.50	1.12	56.18	36.46	2.48	24.14
				SE	6.82	5.54	0.21	1.49	0.74	0.56	0.15	0.34	16.94	10.99	0.75	7.28
				A vs P					**0.03216**				**0.00029**			

Supplementary Table 2. Mitotic activity in the germ rudiment at the time of intercalation line (IL) formation. "Live" samples correspond to lightsheet sample embryos (Supplementary Table 1). Data from samples WT1, WT2 and WT3 were used to generate rose plots in Supplementary Figure 2a.

		Row cell identity																
Experiment	**Sample #**	**L7**	**L6**	**L5**	**L5**	**L3**	**L2**	**L1**	**ML**	**R1**	**R2**	**R3**	**R4**	**R5**	**R6**	**R7**	**Total # En+**	**Sample Mean**
Wild Type	**1**	0.00	0.00	0.00	1.00	1.00	1.00	1.00	1.00	1.00	1.00	1.00	1.00	0.00	0.00	0.00	9	0.60
	2	0.00	0.00	1.00	1.00	1.00	1.00	1.00	1.00	1.00	1.00	1.00	1.00	1.00	0.00	0.00	11	0.73
	3	0.00	0.00	1.00	1.00	1.00	1.00	1.00	1.00	1.00	1.00	1.00	1.00	1.00	0.00	0.00	11	0.73
	4	0.00	0.00	0.00	1.00	1.00	1.00	1.00	1.00	1.00	1.00	1.00	1.00	0.00	0.00	0.00	9	0.60
	5	0.00	0.00	1.00	1.00	1.00	1.00	1.00	1.00	1.00	1.00	1.00	1.00	1.00	0.00	0.00	11	0.73
	6	0.00	0.00	0.00	1.00	1.00	1.00	1.00	1.00	1.00	1.00	1.00	1.00	1.00	0.00	0.00	10	0.67
	7	0.00	0.00	0.00	1.00	1.00	1.00	1.00	1.00	1.00	1.00	1.00	1.00	0.00	0.00	0.00	9	0.60
	8	0.00	0.00	0.00	0.00	1.00	1.00	1.00	1.00	1.00	1.00	1.00	0.00	0.00	0.00	0.00	7	0.47
	9	0.00	0.00	0.00	1.00	1.00	1.00	1.00	1.00	1.00	1.00	1.00	1.00	0.00	0.00	0.00	9	0.60
	10	1.00	1.00	1.00	1.00	1.00	1.00	1.00	1.00	1.00	1.00	1.00	1.00	1.00	0.00	0.00	13	0.87
	11	0.00	0.00	0.00	1.00	1.00	1.00	1.00	1.00	1.00	1.00	1.00	1.00	0.00	0.00	0.00	9	0.60
	12	0.00	0.00	0.00	1.00	1.00	1.00	1.00	1.00	1.00	1.00	1.00	0.00	0.00	0.00	0.00	8	0.53
	Cell Mean	**0.08**	**0.08**	**0.33**	**0.92**	**1.00**	**1.00**	**1.00**	**1.00**	**1.00**	**1.00**	**1.00**	**0.83**	**0.42**	**0.00**	**0.00**	**9.67**	
Lateral Ablation	**1**	0.00	0.00	0.00	1.00	1.00	1.00	1.00	1.00	1.00	1.00	1.00	1.00	0.00	0.00	0.00	9	0.60
	2	0.00	0.00	0.00	0.00	1.00	1.00	1.00	1.00	1.00	1.00	1.00	1.00	0.00	0.00	0.00	8	0.53
	3	0.00	0.00	0.00	0.00	0.00	0.00	1.00	1.00	1.00	1.00	1.00	0.00	0.00	0.00	0.00	5	0.33
	Cell Mean	**0.00**	**0.00**	**0.00**	**0.33**	**0.67**	**0.67**	**1.00**	**1.00**	**1.00**	**1.00**	**1.00**	**0.67**	**0.00**	**0.00**	**0.00**	**7.33**	
Midline Ablation	**1**	0.00	0.00	0.00	1.00	1.00	0.00	1.00	1.00	1.00	1.00	0.00	0.00	0.00	0.00	0.00	6	0.40
	2	0.00	0.00	0.00	0.00	0.00	0.00	0.00	1.00	1.00	1.00	1.00	0.00	0.00	0.00	0.00	4	0.27
	3	0.00	0.00	0.00	0.00	0.00	0.00	0.00	0.00	0.00	0.00	0.00	0.00	0.00	0.00	0.00	0	0.00
	4	0.00	0.00	0.00	0.00	0.00	0.00	0.00	0.00	0.00	0.00	0.00	0.00	0.00	0.00	0.00	0	0.00
	Cell Mean	**0.00**	**0.00**	**0.00**	**0.25**	**0.25**	**0.00**	**0.25**	**0.50**	**0.50**	**0.50**	**0.25**	**0.00**	**0.00**	**0.00**	**0.00**	**2.50**	

Supplementary Table 3. En expression in cells of the prospective mandibular segment in wild type (WT) embryos, following ablation of cell bonds lateral to the midline (Lat), or following ablation of cell bonds at the midline, as depicted in Fig. 6b, c. These data were used to generate Fig. 6e.

1056 **References**
1057

1058 1. His, W. *Untersuchungen über die erste Anlage des Wirbelthierleibes: die erste Entwickelung*
1059 *des Hühnchens im Ei*. (F.C.W. Vogel, Leipzig, 1868).

1060 2. Keller, E. F. *The Century of the Gene*. (Harvard University Press, Cambridge, Massachusetts,
1061 2002).

1062 3. Turing, A. M. The Chemical Basis of Morphogenesis. *Philos. Trans. R. Soc. Lond. Ser. B,*
1063 *Biol. Sci.* **237**, 37–72 (1952).

1064 4. Neumann, C. & Cohen, S. Problems and paradigms: Morphogens and pattern formation.
1065 *BioEssays* **19**, 721–729 (1997).

1066 5. Müller, G. B. & Newman, S. *Origination of Organismal Form: Beyond the Gene in*
1067 *Developmental and Evolutionary Biology*. vol. 2 (MIT Press, Cambridge, Mass, 2003).

1068 6. Roeder, A. H. K. Arabidopsis sepals: A model system for the emergent process of
1069 morphogenesis. *Quant. Plant Biol.* **2**, E14 (2021).

1070 7. Gross, D., Sevrin, A. & Shraiman, B. The Physics of Living Matter: Space, Time and
1071 Information. in *Proceedings of the 27th Solvay Conference on Physics* (eds. Gross, D., Sevrin, A.
1072 & Shraiman, B.) (2020). doi:10.1142/10964.

1073 8. Ghosh, S., Kuyyamudi, C., Steinert, B. L. & Extavour, C. G. Mechanical mechanisms of
1074 morphogenesis as potential substrates for evolutionary change. *Semin. Cell Dev. Biol.* **175**,
1075 103645 (2025).

1076 9. Caldarelli, P. *et al.* Self-organized tissue mechanics underlie embryonic regulation. *Nature*
1077 **633**, 887–894 (2024).

1078 10. Stork, N. E. How Many Species of Insects and Other Terrestrial Arthropods Are There on
1079 Earth? *Annu. Rev. Entomol.* **63**, 1–15 (2017).

1080 11. Brusca, R. C., Moore, W. & Shuster, S. M. Chapter 23: Phylum Arthropoda. in *The*
1081 *Invertebrates. Third Edition* (Sinauer Associates, Sunderland, MA, USA, 2016).

1082 12. Clark, E., Peel, A. D. & Akam, M. Arthropod segmentation. *Development* **146**, dev170480
1083 (2019).

1084 13. Buckley, C. E. & Johnston, D. S. Apical–basal polarity and the control of epithelial form and
1085 function. *Nat. Rev. Mol. Cell Biol.* **23**, 559–577 (2022).

1086 14. Classen, A.-K., Anderson, K. I., Marois, E. & Eaton, S. Hexagonal Packing of *Drosophila*
1087 Wing Epithelial Cells by the Planar Cell Polarity Pathway. *Dev. Cell* **9**, 805–817 (2005).

1088 15. Gibson, M. C., Patel, A. B., Nagpal, R. & Perrimon, N. The emergence of geometric order in
1089 proliferating metazoan epithelia. *Nature* **442**, 1038–1041 (2006).

1090 16. Farhadifar, R., Röper, J.-C., Aigouy, B., Eaton, S. & Jülicher, F. The influence of cell
1091 mechanics, cell-cell interactions, and proliferation on epithelial packing. *Curr. Biol.* **17**, 2095–
1092 2104 (2007).

1093 17. Bardet, P.-L. *et al.* PTEN controls junction lengthening and stability during cell
1094 rearrangement in epithelial tissue. *Dev. Cell* **25**, 534–546 (2013).

1095 18. Nagpal, R., Patel, A. & Gibson, M. C. Epithelial topology. *BioEssays* **30**, 260–266 (2008).

1096 19. Monier, B., Pélissier-Monier, A., Brand, A. H. & Sanson, B. An actomyosin-based barrier
1097 inhibits cell mixing at compartmental boundaries in Drosophila embryos. *Nature Cell Biol.* **12**,
1098 60–69 (2010).

1099 20. Simone, R. P. & DiNardo, S. Actomyosin contractility and Discs large contribute to
1100 junctional conversion in guiding cell alignment within the Drosophila embryonic epithelium.
1101 *Development* **137**, 1385–1394 (2010).

1102 21. Wright, D. A. & Lawrence, P. A. Regeneration of segment boundaries in Oncopeltus: Cell
1103 lineage. *Dev. Biol.* **85**, 328–333 (1981).

1104 22. Zallen, J. A. & Zallen, R. Cell-pattern disordering during convergent extension in
1105 Drosophila. *J. Phys.: Condens. Matter* **16**, S5073–S5080 (2004).

1106 23. Honda, H. Geometrical Models for Cells in Tissues. *Int. Rev. Cyt.* **81**, 191–248 (1983).

1107 24. Tamada, M. & Zallen, J. A. Square Cell Packing in the Drosophila Embryo through
1108 Spatiotemporally Regulated EGF Receptor Signaling. *Dev. Cell* **35**, 151–161 (2015).

1109 25. Dohle, W., Gerberding, M., Hejnol, A. & Scholtz, G. Cell lineage, segment differentiation,
1110 and gene expression in crustaceans. in *Evolutionary Developmental Biology of Crustacea* (ed.
1111 Scholtz, G.) 95–133 (A.A. Balkema, Lisse, 2004).

1112 26. Gerberding, M. & Scholtz, G. Cell lineage of the midline cells in the amphipod crustacean
1113 Orchestia cavimana (Crustacea, Malacostraca) during formation and separation of the germ
1114 band. *Dev. Genes Evol.* **209**, 91–102 (1999).

1115 27. Gerberding, M., Browne, W. E. & Patel, N. H. Cell lineage analysis of the amphipod
1116 crustacean Parhyale hawaiensis reveals an early restriction of cell fates. *Development* **129**, 5789–
1117 5801 (2002).

1118 28. Scholtz, G. & Dohle, W. Cell lineage and cell fate in crustacean embryos--a comparative
1119 approach. *Int. J. Dev. Biol.* **40**, 211–20 (1996).

1120 29. Browne, W. E., Price, A. L., Gerberding, M. & Patel, N. H. Stages of embryonic
1121 development in the amphipod crustacean Parhyale hawaiensis. *genesis* **42**, 124–149 (2005).

1122 30. Spencer, M. A., Jabeen, Z. & Lubensky, D. K. Vertex stability and topological transitions in
1123 vertex models of foams and epithelia. *Eur. Phys. J. E* **40**, 1–17 (2017).

1124 31. Sun, D. A. & Patel, N. H. The amphipod crustacean Parhyale hawaiensis: An emerging
1125 comparative model of arthropod development, evolution, and regeneration. *Wiley Interdiscip.*
1126 *Rev. Dev. Biol.* **8**, e355 (2019).

1127 32. Lawrence, P. A. *The Making of a Fly: The Genetics of Animal Design*. (Wiley-Blackwell,
1128 New Jersey, USA, 1992).

1129 33. Alwes, F., Hinchen, B. & Extavour, C. G. Patterns of cell lineage, movement, and migration
1130 from germ layer specification to gastrulation in the amphipod crustacean Parhyale hawaiensis.
1131 *Dev. Biol.* **359**, 110–123 (2011).

1132 34. Cislo, D. J. *et al.* Active cell divisions generate fourfold orientationally ordered phase in
1133 living tissue. *Nat. Phys.* **19**, 1201–1210 (2023).

1134 35. Extavour, C. G. The fate of isolated blastomeres with respect to germ cell formation in the
1135 amphipod crustacean Parhyale hawaiensis. *Dev. Biol.* **277**, 387–402 (2005).

1136 36. Chaw, R. C. & Patel, N. H. Independent migration of cell populations in the early
1137 gastrulation of the amphipod crustacean Parhyale hawaiensis. *Dev. Biol.* **371**, 94–109 (2012).

1138 37. Patel, N. H. *et al.* Expression of *engrailed* proteins in arthropods, annelids, and chordates.
1139 *Cell* **58**, 955–968 (1989).

1140 38. Heemskerk, I. & Streichan, S. J. Tissue cartography: compressing bio-image data by
1141 dimensional reduction. *Nat. Methods* **12**, 1139–1142 (2015).

1142 39. Keller, R. E. & Trinkaus, J. P. Rearrangement of enveloping layer cells without disruption of
1143 the epithelial permeability barrier as a factor in Fundulus epiboly. *Dev. Biol.* **120**, 12–24 (1987).

1144 40. Price, A. L., Modrell, M. S., Hannibal, R. L. & Patel, N. H. Mesoderm and ectoderm lineages
1145 in the crustacean Parhyale hawaiensis display intra-germ layer compensation. *Dev. Biol.* **341**,
1146 256–266 (2010).

1147 41. Graner, F. & Glazier, J. A. Simulation of biological cell sorting using a two-dimensional
1148 extended Potts model. *Phys. Rev. Lett.* **69**, 2013–2016 (1992).

1149 42. Holtfreter, J. Tissue Affinity, A Means of Embryonic Morphogenesis. in *Foundations of*
1150 *Experimental Embryology* (eds. Willier, B. H. & Oppenheimer, J. M.) 186–225 (Prentice-Hall,
1151 Englewood Cliffs, N.J., 1939).

1152 43. Swat, M. H. *et al.* Multi-Scale Modeling of Tissues Using CompuCell3D. *Methods Cell Biol.*
1153 **110**, 325–366 (2012).

1154 44. Scholtz, G., Patel, N. H. & Dohle, W. Serially homologous engrailed stripes are generated
1155 via different cell lineages in the germ band of amphipod crustaceans (Malacostraca, Peracarida).
1156 *Int. J. Dev. Biol.* **38**, 471–8 (1994).

1157 45. Scholtz, G. The formation, differentiation and segmentation of the post-naupliar germ band
1158 of the amphipod Gammarus pulex L. (Crustacea, Malacostraca, Peracarida). *Proc. R. Soc. Lond.*
1159 *B* **239**, 163–211 (1990).

1160 46. Wolff, C. & Scholtz, G. Cell Lineage, Axis Formation, and the Origin of Germ Layers in the
1161 Amphipod Crustacean Orchestia cavimana. *Dev. Biol.* **250**, 44–58 (2002).

1162 47. Gerberding, M. & Scholtz, G. Neurons and Glia in the Midline of the Higher Crustacean
1163 Orchestia cavimana Are Generated via an Invariant Cell Lineage That Comprises a Median
1164 Neuroblast and Glial Progenitors. *Dev. Biol.* **235**, 397–409 (2001).

1165 48. Fischer, A. H. L., Pabst, T. & Scholtz, G. Germ band differentiation in the stomatopod
1166 Gonodactylaceus falcatus and the origin of the stereotyped cell division pattern in Malacostraca
1167 (Crustacea). *Arthropod Struct. Dev.* **39**, 411–422 (2010).

1168 49. Scholtz, G. & Wolff, C. Cleavage, gastrulation, and germ disc formation of the amphipod
1169 Orchestia cavimana (Crustacea, Malacostraca, Peracarida). *Contrib. Zool.* **71**, 9–28 (2002).

1170 50. Keller, R. *et al.* Mechanisms of convergence and extension by cell intercalation. *Philos.*
1171 *Trans. R. Soc. Lond.* **355**, 897–922 (2000).

1172 51. Karess, R. E. *et al.* The regulatory light chain of nonmuscle myosin is encoded by spaghetti-
1173 squash, a gene required for cytokinesis in Drosophila. *Cell* **65**, 1177–1189 (1991).

1174 52. Landsberg, K. P. *et al.* Increased Cell Bond Tension Governs Cell Sorting at the Drosophila
1175 Anteroposterior Compartment Boundary. *Curr. Biol.* **19**, 1950–1955 (2009).

1176 53. Scarpa, E., Finet, C., Blanchard, G. B. & Sanson, B. Actomyosin-Driven Tension at
1177 Compartmental Boundaries Orients Cell Division Independently of Cell Geometry In Vivo. *Dev*
1178 *Cell* **47**, 727-740.e6 (2018).

1179 54. Jain, A. *et al.* Regionalized tissue fluidization is required for epithelial gap closure during
1180 insect gastrulation. *Nat. Commun.* **11**, 5604 (2020).

1181 55. Martin, A. C. The Physical Mechanisms of Drosophila Gastrulation: Mesoderm and
1182 Endoderm Invagination. *Genetics* **214**, 543–560 (2020).

1183 56. Parzen, E. On Estimation of a Probability Density Function and Mode. *Ann. Math. Stat.* **33**,
1184 1065–1076 (1962).

1185 57. Rosenblatt, M. Remarks on Some Nonparametric Estimates of a Density Function. *Ann.*
1186 *Math. Stat.* **27**, 832–837 (1956).

1187 58. Townes, P. L. & Holtfreter, J. Directed movements and selective adhesion of embryonic
1188 amphibian cells. *J. Exp. Zool.* **128**, 53–120 (1955).

1189 59. García-Bellido, A. Pattern reconstruction by dissociated imaginal disk cells of *Drosophila*
1190 *melanogaster*. *Dev. Biol.* **14**, 278–306 (1966).

1191 60. McMillen, P. & Holley, S. A. Integration of cell–cell and cell–ECM adhesion in vertebrate
1192 morphogenesis. *Curr. Opin. Cell Biol.* **36**, 48–53 (2015).

1193 61. Skamrahl, M. *et al.* Cellular segregation in cocultures is driven by differential adhesion and
1194 contractility on distinct timescales. *Proc. Natl. Acad. Sci.* **120**, e2213186120 (2023).

1195 62. Maitre, J.-L. *et al.* Adhesion Functions in Cell Sorting by Mechanically Coupling the
1196 Cortices of Adhering Cells. *Science* **338**, 253–256 (2012).

1197 63. Bao, M. *et al.* Stem cell-derived synthetic embryos self-assemble by exploiting cadherin
1198 codes and cortical tension. *Nat. Cell Biol.* **24**, 1341–1349 (2022).

1199 64. Steinberg, M. S. Adhesion-guided multicellular assembly: a commentary upon the postulates,
1200 real and imagined, of the differential adhesion hypothesis, with special attention to computer
1201 simulations of cell sorting. *J. Theor. Biol.* **55**, 431–443 (1975).

1202 65. Tepass, U., Godt, D. & Winklbauer, R. Cell sorting in animal development: signalling and
1203 adhesive mechanisms in the formation of tissue boundaries. *Curr. Opin. Genet. Dev.* **12**, 572–
1204 582 (2002).

1205 66. Iijima, N., Sato, K., Kuranaga, E. & Umetsu, D. Differential cell adhesion implemented by
1206 Drosophila Toll corrects local distortions of the anterior-posterior compartment boundary. *Nat.*
1207 *Commun.* **11**, 6320 (2020).

1208 67. Hogeweg, P. Evolving Mechanisms of Morphogenesis: on the Interplay between Differential
1209 Adhesion and Cell Differentiation. *J. Theor. Biol.* **203**, 317–333 (2000).

1210 68. Blankenship, J. T., Backovic, S. T., Sanny, J. S. P., Weitz, O. & Zallen, J. A. Multicellular
1211 rosette formation links planar cell polarity to tissue morphogenesis. *Dev. Cell* **11**, 459–470
1212 (2006).

1213 69. Jacinto, A. *et al.* Dynamic analysis of actin cable function during Drosophila dorsal closure.
1214 *Curr. Biol.* **12**, 1245–1250 (2002).

1215 70. Martin, P. & Lewis, J. Actin cables and epidermal movement in embryonic wound healing.
1216 *Nature* **360**, 179–183 (1992).

1217 71. Maroudas-Sacks, Y. *et al.* Topological defects in the nematic order of actin fibres as
1218 organization centres of Hydra morphogenesis. *Nat. Phys.* **17**, 251–259 (2021).

1219 72. Calzolari, S., Terriente, J. & Pujades, C. Cell segregation in the vertebrate hindbrain relies on
1220 actomyosin cables located at the interhombomeric boundaries. *EMBO J.* **33**, 686–701 (2014).

1221 73. Saadaoui, M., Rocancourt, D., Roussel, J., Corson, F. & Gros, J. A tensile ring drives tissue
1222 flows to shape the gastrulating amniote embryo. *Science* **367**, 453–458 (2020).

1223 74. Lee, J.-Y. *et al.* Wnt/Frizzled Signaling Controls C. elegans Gastrulation by Activating
1224 Actomyosin Contractility. *Curr. Biol.* **16**, 1986–1997 (2006).

1225 75. Serra, M. *et al.* A mechanochemical model recapitulates distinct vertebrate gastrulation
1226 modes. *Sci. Adv.* **9**, eadh8152 (2023).

1227 76. Lienkamp, S. S. *et al.* Vertebrate kidney tubules elongate using a planar cell polarity-
1228 dependent, rosette-based mechanism of convergent extension. *Nat. Genet.* **44**, 1382–1387
1229 (2012).

1230 77. Ybot-Gonzalez, P. *et al.* Convergent extension, planar-cell-polarity signalling and initiation
1231 of mouse neural tube closure. *Development* **134**, 789–799 (2007).

1232 78. Darken, R. S. *et al.* The planar polarity gene strabismus regulates convergent extension
1233 movements in Xenopus. *EMBO J.* **21**, 976–985 (2002).

1234 79. Williams, M. L. & Solnica-Krezel, L. Nodal and planar cell polarity signaling cooperate to
1235 regulate zebrafish convergence and extension gastrulation movements. *eLife* **9**, e54445 (2020).

1236 80. Goto, T. & Keller, R. The Planar Cell Polarity Gene Strabismus Regulates Convergence and
1237 Extension and Neural Fold Closure in Xenopus. *Dev. Biol.* **247**, 165–181 (2002).

1238 81. Gallagher, K. D., Mani, M. & Carthew, R. W. Emergence of a geometric pattern of cell fates
1239 from tissue-scale mechanics in the Drosophila eye. *eLife* **11**, e72806 (2022).

1240 82. Dicko, M. *et al.* Geometry can provide long-range mechanical guidance for embryogenesis.
1241 *PLoS Comput. Biol.* **13**, e1005443 (2017).

1242 83. Guignard, L. *et al.* Contact area–dependent cell communication and the morphological
1243 invariance of ascidian embryogenesis. *Science* **369**, eaar5663 (2020).

1244 84. Royer, C. *et al.* Establishment of a relationship between blastomere geometry and YAP
1245 localisation during compaction. *Development* **147**, dev189449 (2020).

1246 85. Kumar, A. & Shivashankar, G. V. Mechanical Force Alters Morphogenetic Movements and
1247 Segmental Gene Expression Patterns during Drosophila Embryogenesis. *PLoS ONE* **7**, e33089
1248 (2012).

1249 86. Ho, M. W., Matheson, A., Saunders, P. T., Goodwin, B. C. & Smallcombe, A. Ether-induced
1250 segmentation disturbances in Drosophila melanogaster. *Roux's Arch. Dev. Biol.* **196**, 511–521
1251 (1987).

1252 87. Dohle, W. & Scholtz, G. Clonal analysis of the crustacean segment: the discordance between
1253 genealogical and segmental borders. *Development* **104**, 147–160 (1988).

1254 88. Scholtz, G. From a Single Cell to Segmental Structures: Crustacean Embryology. in (Oxford
1255 University Press, 2020).

1256 89. Scholtz, G. Evolution of the nauplius stage in malacostracan crustaceans. *J. Zool. Syst. Evol.*
1257 *Res.* **38**, 175–187 (2000).

1258 90. Gupta, T. & Extavour, C. G. Identification of a putative germ plasm in the amphipod
1259 Parhyale hawaiensis. *EvoDevo* **4**, 34 (2013).

1260 91. Nestorov, P., Battke, F., Levesque, M. P. & Gerberding, M. The Maternal Transcriptome of
1261 the Crustacean Parhyale hawaiensis Is Inherited Asymmetrically to Invariant Cell Lineages of
1262 the Ectoderm and Mesoderm. *PLoS ONE* **8**, e56049 (2013).

1263 92. Scholtz, G. Chapter 24: Cleavage, germ band formation and head segmentation: the ground
1264 pattern of the Euarthropoda. in *Arthropod Relationships* (eds. Fortey, R. A. & Thomas, R. H.)
1265 317–332 (Chapman & Hall, London, UK, 1997).

1266 93. Scholtz, G. & Wolff, C. Chapter 4: Arthropod Embryology: Cleavage and Germ Band
1267 Development. in *Arthropod Biology and Evolution* (ed. Minelli, A.) 63–89 (2013).
1268 doi:10.1007/978-3-642-36160-9_4.

1269 94. Wolff, C. *et al.* Multi-view light-sheet imaging and tracking with the MaMuT software
1270 reveals the cell lineage of a direct developing arthropod limb. *eLife* **7**, e34410 (2018).

1271 95. Kontarakis, Z. & Pavlopoulos, A. Chapter 10. Transgenesis in Non-model Organisms: The
1272 Case of Parhyale. in *Hox Genes: Methods and Protocols* (eds. Graba, Y. & Rezsohazy, R.) vol.
1273 1196 145–181 (Humana Press, New York, NY, 2014).

1274 96. Riedl, J. *et al.* Lifeact: a versatile marker to visualize F-actin. *Nat. Methods* **5**, 605–607
1275 (2008).

1276 97. Shaner, N. C. *et al.* A bright monomeric green fluorescent protein derived from
1277 Branchiostoma lanceolatum. *Nat. Methods* **10**, 407–409 (2013).

1278 98. Pavlopoulos, A., Berghammer, A. J., Averof, M. & Klingler, M. Efficient Transformation of
1279 the Beetle Tribolium castaneum Using the Minos Transposable Element Quantitative and
1280 Qualitative Analysis of Genomic Integration Events. *Genetics* **167**, 737–746 (2004).

1281 99. Özpolat, B. D., Handberg-Thorsager, M., Vervoort, M. & Balavoine, G. Cell lineage and cell
1282 cycling analyses of the 4d micromere using live imaging in the marine annelid Platynereis
1283 dumerilii. *eLife* **6**, e30463 (2017).

1284 100. Vopalensky, P., Tosches, M. A., Achim, K., Handberg-Thorsager, M. & Arendt, D. From
1285 spiral cleavage to bilateral symmetry: the developmental cell lineage of the annelid brain. *BMC*
1286 *Biol.* **17**, 81 (2019).

1287 101. Rehm, E. J., Hannibal, R. L., Chaw, R. C., Vargas-Vila, M. & Patel, N. H. Fixation and
1288 dissection of Parhyale hawaiensis embryos. *Cold Spring Harb. Protoc.* **2009**, pdb.prot5127
1289 (2009).

1290 102. Kiehart, D. P. & Feghali, R. Cytoplasmic myosin from Drosophila melanogaster. *J. Cell*
1291 *Biol.* **103**, 1517–1525 (1986).

1292 103. Tomer, R., Khairy, K., Amat, F. & Keller, P. J. Quantitative high-speed imaging of entire
1293 developing embryos with simultaneous multiview light-sheet microscopy. *Nat. Methods* **9**, 755–
1294 763 (2012).

1295 104. Pietzsch, T., Saalfeld, S., Preibisch, S. & Tomancak, P. BigDataViewer: visualization and
1296 processing for large image data sets. *Nat. Methods* **12**, 481–483 (2015).

1297 105. Preibisch, S., Saalfeld, S., Schindelin, J. & Tomancak, P. Software for bead-based
1298 registration of selective plane illumination microscopy data. *Nat. Methods* **7**, 418–419 (2010).

1299 106. Preibisch, S. *et al.* Efficient Bayesian-based multiview deconvolution. *Nat. Methods* **11**,
1300 645–648 (2014).

1301 107. Schindelin, J. *et al.* Fiji: an open-source platform for biological-image analysis. *Nat.*
1302 *Methods* **9**, 676–82 (2012).

1303 108. Berg, S. *et al.* ilastik: interactive machine learning for (bio)image analysis. *Nature Methods*
1304 **16**, 1226–1232 (2019).

1305 109. Heemskerk, I. & Streichan, S. J. Tissue cartography: compressing bio-image data by
1306 dimensional reductio n. *Nature Methods* **12**, 1139–1142 (2015).

1307 110. Etournay, R. *et al.* TissueMiner: A multiscale analysis toolkit to quantify how cellular
1308 processes create tissue dynamics. *eLife* **5**, e14334 (2016).

1309 111. Stringer, C. & Pachitariu, M. Cellpose3: one-click image restoration for improved cellular
1310 segmentation. *bioRxiv* 2024.02.10.579780 (2024) doi:10.1101/2024.02.10.579780.

1311 112. Glazier, J. A. & Graner, F. Simulation of the differential adhesion driven rearrangement of
1312 biological cells. *Phys. Rev. E* **47**, 2128–2154 (1993).

113. Aigouy, B., Umetsu, D. & Eaton, S. Segmentation and Quantitative Analysis of Epithelial Tissues. in *Methods in Molecular Biology: Drosophila Methods and Protocols* (ed. Dahlmann, C.) vol. 1478 227–239 (Springer New York, New York, NY, 2016).